Evolution of microstructure and melt topology in partially molten granitic mylonite: Implications for rheology of felsic middle crust.

K. Schulmann, J. Martelat, S. Ulrich, O. Lexa, P. Stipska, J.K. Becker

Evolution of microstructure and melt topology in partially molten granitic mylonite: Implications for rheology of felsic middle crust

Karel Schulmann,[1] Jean-Emmanuel Martelat,[2] Stanislav Ulrich,[3,4] Ondrej Lexa,[4] Pavla Štípská,[1] and Jens K. Becker[5]

Received 19 November 2007; revised 27 April 2008; accepted 30 July 2008; published 24 October 2008.

[1] The deformation study of midcrustal porphyritic granite reveals exceptionally high strain intensities of feldspar aggregates compared to stronger quartz. Three types of microstructures corresponding to evolutionary stages of deformed granite were recognized: (1) the metagranite marked by viscous flow of plagioclase around strong alkali feldspar and quartz, (2) quartz augen orthogneiss characterized by development of banded mylonitic structure of recrystallized plagioclase and K-feldspar surrounding augens of quartz, and (3) banded mylonite characterized by alternation of quartz ribbons and mixed aggregates of feldspars and quartz. The original weakening of alkali feldspar is achieved by decomposition into albite chains and K-feldspar resulting from a heterogeneous nucleation process. The subsequent collapse of alkaline feldspar and development of monomineralic layering is attributed to the onset of syn-deformational dehydration melting of Mu-Bi layers associated with production of ~2% melt. The final deformation stage is marked by mixing of feldspars which is explained by higher melt production due to introduction of external water. An already small amount of melt is responsible for extreme weakening of the feldspar because of Melt Connectivity Threshold effect triggering grain boundary sliding deformation mechanisms. The grain boundary sliding controls diffusion creep at small melt fraction and evolves to particulate flow at high melt fractions. Strong quartz shows a dislocation creep deformation mechanism throughout the whole deformation history marked by variations in the activity of the slip systems, which are attributed to variations in stress and strain rate partitioning with regard to changing rheological properties of the deforming feldspars.

Citation: Schulmann, K., J.-E. Martelat, S. Ulrich, O. Lexa, P. Štípská, and J. K. Becker (2008), Evolution of microstructure and melt topology in partially molten granitic mylonite: Implications for rheology of felsic middle crust, *J. Geophys. Res.*, *113*, B10406, doi:10.1029/2007JB005508.

1. Introduction

[2] Rheology of the continental crust is dominated by quartzo-feldspathic rocks, which are represented mainly by metagranitoids, orthogneisses and felsic volcanics [*Carter and Tsenn*, 1987]. To date, the models of crustal rheology use laboratory derived laws described by constitutive equations that are established for minerals or monomineralic rocks such as quartzites and anorthosites [*Ranalli*, 1995]. Most of laboratory experiments show that the quartz is weaker than plagioclase for the same homologous temperatures [*Ranalli and Murphy*, 1987; *Schmid*, 1982]. However, the natural quartzo-feldspathic rocks are mixtures with different proportions of strong feldspars and weak quartz with variable grain shapes and grain size distributions. The deformation of such natural rocks leads to strain partitioning between the different components and nonuniform deformation [*Handy*, 1990]. *Handy* [1994a] defined the load-bearing framework structure and interconnected weak layer structure and proposed comprehensive empirical equations that determine the strength of polyphase composites. *Handy* [1994a] applied this concept to quartzo-feldspathic rocks and concluded that the proportion of weaker quartz controls the bulk rheology. The basis of these models is the coexistence of two nonlinear viscous phases; the bulk rheology is a consequence of the rock structure and the relative proportions of the two mineral phases [*Ji and Zhao*, 1994].

[3] Microstructural studies show that the progressive orthogneiss deformation is associated with strain partitioning and variations in the deformation mechanisms of feldspars and quartz [*Handy et al.*, 1999; *Schulmann et al.*, 1996; *Simpson*, 1985]. For instance *Gapais* [1989] and

[1]Centre de Géochimie de la Surface, UMR7516, Université Louis Pasteur, CNRS, Strasbourg, France.
[2]Laboratoire de Géodynamique des Chaînes Alpines, UMR5025, Université Joseph Fourier, Observatoire des Sciences de l'Univers de Grenoble, CNRS, Grenoble, France.
[3]Geophysical Institute, Czech Academy of Sciences, Prague, Czech Republic.
[4]Institute of Petrology and Structural Geology, Charles University, Prague, Czech Republic.
[5]Institut für Geowissenschaften, Universität Tübingen, Tübingen, Germany.

0148-0227/08/2007JB005508$09.00

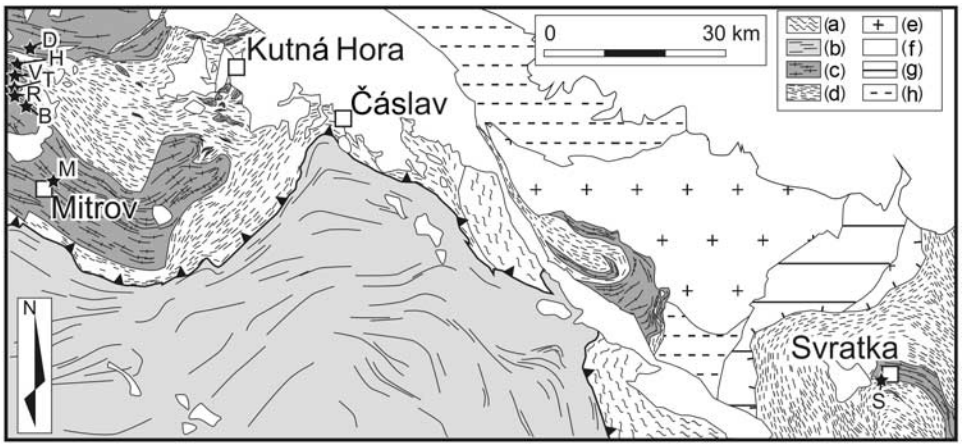

Figure 1. Geological map of the central part of Bohemian Massif modified after *Beneš* [1964] and *Synek and Oliverová* [1993]. Black stars and capitalized letters refer to studied samples (B, D, H, M, R, S, T, and V). (a) Lower crustal rocks (granulites and eclogites), (b) the midcrustal monotonous metasedimentary unit, (c) the midcrustal orthogneiss unit, (d) the kyanite micaschist unit, (e) the intrusives, (f) Cretaceous and Quaternary rocks, (g) the undifferenciated Lower Palaeozoic rocks, and (h) the Neo-Proterozoic metasediments.

Schulmann et al. [1996] have shown that at amphibolite facies the feldspars show evolution from dislocation creep to grain boundary sliding with increasing strain intensity in conjunction with variations in the activity of the quartz slip systems. Therefore, the viscosity contrast between feldspars and quartz was not constant but varied with increasing degree of strain as the rheological role of individual minerals evolved as shown by a range of experimental and natural studies [*Handy*, 1994b; *Ji et al.*, 2000; *Rybacki and Dresen*, 2004; *Stünitz and Fitz Gerald*, 1993]. However, the aforementioned studies all neglect a possible role of the melt on the deformation of the polyphase rocks.

[4] The aim of this paper is to show, through detailed microstructural study and thermodynamical modeling, the contribution of interstitial melt to the rheology of progressively deformed granites under midcrustal conditions. We use natural examples of a sequence of granite mylonites to document the melt enhanced rheological inversion of disproportionately stronger quartz compared to the weak feldspars in midcrustal rocks. This work also shows that with increasing melt fraction the deformation mechanisms of feldspars varies from the grain boundary sliding accommodated dislocation creep to granular flow while the quartz is only deformed in the dislocation creep field.

2. Geological Setting

[5] The study area located in the central part of the Bohemian Massif in the Czech Republic is known for the extreme deformation of porphyritic granites in a crustal-scale shear zone [*Synek and Oliverová*, 1993]. The porphyritic granite mylonites studied are of Cambro-Ordovician protolith age and come from an orthogneiss-bearing, midcrustal unit that overlies kyanite micaschists in the west (Figure 1). In the east a similar rock assemblage occurs in an equivalent structural unit, although these orthogneiss bodies exist within kyanite-sillimanite bearing micaschists. According to *Schulmann et al.* [2005] both units record a Carboniferous tectono-metamorphic history between 340 and 325 Ma. The midcrustal unit is overlain by kyanite bearing migmatites and granulites of the orogenic lower crustal unit that contain eclogite lenses with estimated minimum pressures of 18–19 kbar and temperatures of 800–900°C [*Medaris et al.*, 1998]. The P-T conditions of the kyanite bearing micaschists in the footwall of the mylonitic orthogneiss sheet have experienced temperatures of 620–710°C at pressures of 6.5–9.5 kbar [*Kachlík*, 1999] similarly to 8–9 kbar and 610–660°C estimated in the micaschists in the eastern part of the studied area [*Pitra and Guiraud*, 1996].

[6] The geological structure of the studied rocks was described by *Synek and Oliverová* [1993] who interpreted the middle crustal orthogneiss-bearing unit and the overlying orogenic lower crustal unit as a crustal nappe stack resulting from a Carboniferous deformation. On the basis of the structural position of the midcrustal orthogneiss and the regional metamorphic field gradient, the PT conditions of metamorphism and deformation of the studied rocks are estimated to be between 9 and 18 kbar and 650–850°C. More precise P-T estimations were not established because of the lack of pressure and temperature sensitive mineral assemblages that are necessary for standard thermobarometric methods.

3. Shape Analysis of Quartz and Feldspars

[7] Undeformed porphyritic granitoids may serve as an excellent example of multiphase mixtures of originally spherical (ellipsoidal) clasts with constant phase fractions. When these rocks are subjected to deformation, mineral grains reach different strain intensities, which can be easily quantified using standard finite strain techniques [*Ramsay and Huber*, 1983]. Measurement of the shapes of naturally deformed minerals in originally coarse-grained and porphyritic granitoids may thus help to track the viscous behavior of individual phases for different bulk strain intensities

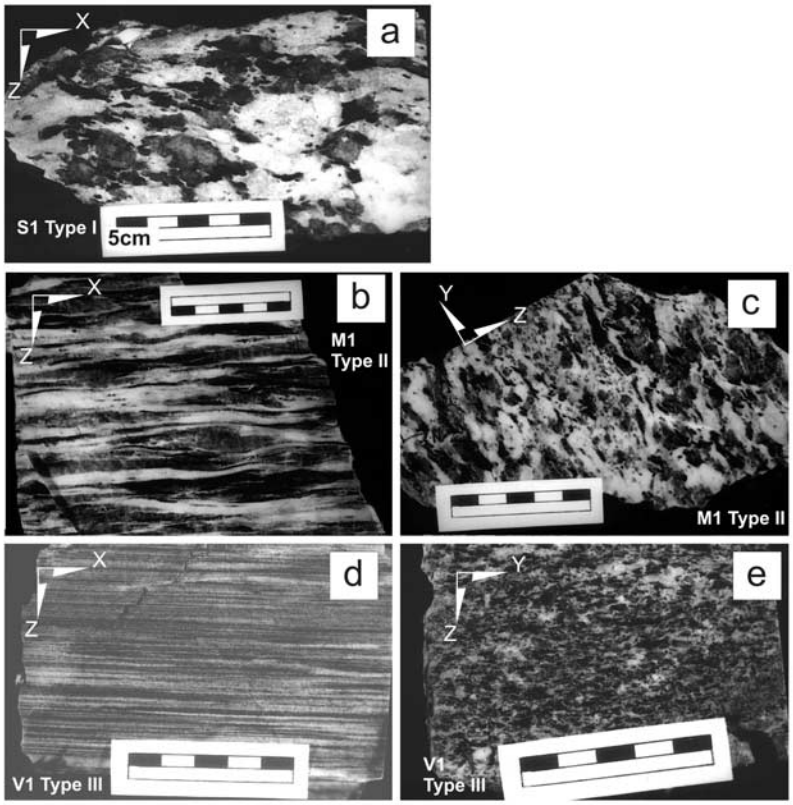

Figure 2. Macroscopic samples of deformed metagranite divided in three types according to the deformation intensity and the macroscopic appearance. X, Y, and Z refer to the axes of the finite strain ellipsoid. (a) Sample S1 is a weakly deformed metagranite with large centimeter-sized grains of quartz and feldspar representing Type I rock. (b, c) Sample M1 is an augen orthogneiss corresponding to Type II rocks and intermediate strain intensity (equivalent to samples T1, T2, M2, and R4), (d, e) Sample V1 is a banded mylonite corresponding to Type III rock and the highest intensity of deformation (equivalent to other highly strained samples R5, R3, V2, and H1).

[*Treagus*, 2002]. This allows constraining the degree of strain partitioning in rocks and the viscosity ratios between the individual mineral phases.

[8] The shape analysis of the feldspars and the quartz polycrystalline aggregates was carried out on 17 sections cut both perpendicular to the foliation and parallel to the stretching lineation and perpendicular to both the foliation and the lineation, i.e., parallel to the XZ and YZ sections of the finite strain ellipsoid (Figure 2). The K-feldspar cannot be distinguished from plagioclase in highly deformed macroscopic samples and therefore both minerals were grouped together for finite strain measurements. All studied samples are composed on average of 60–70% feldspars, 35–25% quartz and up to 10% of biotite and muscovite. The almost constant mineral composition for highly variable strain intensities and constant bulk rock chemistry shows the lack of chemical variations with strain (Table 1).

[9] In our study we classified three major types of deformed orthogneiss according to the deformation intensities at the macroscopic scale: Type I is represented by weakly deformed metagranite (Figure 2a); Type II corresponds to augen orthogneiss with quartz porphyroclast (Figures 2b and 2c); Type III is a banded mylonite orthogneiss (Figures 2d and 2e).

[10] Mineral shape data are plotted into a Flinn diagram [*Flinn*, 1965] (Figure 3). The analyses of feldspar polycrystalline aggregates and quartz of the individual samples are connected by tie lines with the vertical ellipse representing the bulk strain value of the whole rock. An important feature of all the studied samples is that feldspars show higher strain intensities than quartz for any bulk strain (Figures 3a and 3b). In several samples of the so-called Doubravčany pencil gneiss, the strain intensities cannot be identified because the stretching of feldspar and quartz layers exceeds the length of the samples (Figure 2d). The strain symmetry, represented by the K values of *Flinn* [1965], varies from prolate to oblate shapes (K = 2.7 to 0.3). For quartz with prolate shapes, the corresponding feldspar strain symmetry is close to plane strain, while for oblate quartz, the feldspars show the same shape or slightly more oblate shapes (Figure 3b). Strain intensities are expressed using Ramsay's D value, which is an alternative expression of viscosity ratio values of *Gay* [1968a, 1968b] also used by *Schulmann et al.* [1996]. The inspection of the diagram in Figure 3b shows that the highest strain ratios are achieved between D_{fel}/D_{qtz} for Type III orthogneiss and some Type II orthogneiss samples marked by high bulk strain intensities. The relatively small ratio between D_{fel}/D_{qtz} suggests similar yield-

Table 1. Bulk Rock Chemistry of Midcrustal Orthogneisses

Sample	S1	M1	V1	D1
SiO_2	72, 9	70, 9	73, 0	70, 2
TiO_2	0, 3	0, 3	0, 2	0, 4
Al_2O_3	13, 3	14, 7	13, 7	14, 7
Fe_2O_3	1, 9	1, 4	1, 8	2, 6
FeO	0, 9	1, 0	0, 7	0, 7
MnO	0, 0	0, 1	0, 0	0, 0
MgO	0, 5	0, 6	0, 4	0, 8
CaO	1, 1	1, 4	0, 8	1, 0
Na_2O	2, 3	2, 6	2, 5	1, 8
K_2O	4, 5	4, 7	4, 7	4, 6
P_2O_5	0, 2	0, 2	0, 2	0, 2
H_2O-	0, 2	0, 3	0, 3	0, 2
H_2O^+	1, 0	1, 2	1, 0	2, 1
CO_2	0, 2	0, 2	0, 4	0, 2
Total	99, 5	99, 5	99, 7	99, 6

ing of both mineral phases for low bulk strains for several samples of weakly deformed Type II orthogneiss.

4. Microstructure Development of Deformed Metagranitoids

[11] The microstructural investigations covered the qualitative description of the rock and mineral structure using optical microscope and scanning electron microscope imaging. The microprobe work complements the scanning electron microscope (SEM) study to identify compositional variations of the recrystallized feldspars (Tables 2a, 2b, and 2c).

4.1. Type I: Metagranite and Weakly Deformed Orthogneiss

[12] The metagranite samples show K-feldspar phenocrysts up to 10 cm in size surrounded by quartz blebs. Elongated plagioclase polycrystalline aggregates range from 1 to 3 cm in size (Figure 2a). Light and SEM microscopies show that the plagioclase forming recrystallized aggregates (labeled Pl1 in Figure 4) corresponds to oligoclase An_{15}. The Pl1 plagioclase has an average grain size of 50 -70 μm, straight boundaries and subequant shapes (Figure 4 and Table 2c). The quartz blebs consist of large grains ($\sim$400 μm in size) with irregular and highly serrated boundaries. Biotite and muscovite are present as elongated recrystallized aggregates. The plagioclase grains within alkaline feldspar phenocrysts are labeled Pl1b here. These plagioclases are 10 to 50 μm in size, correspond to albite An_{1-8} and are usually arranged into chains mostly parallel to (100) or locally along (010) planes of the host K-feldspar (Figures 4a and 4b and Table 2c). The K-feldspars themselves show subgrains of $\sim$80 μm in size. Subgrain boundaries are straight and meet in triple point junctions. At a smaller scale, the feldspars show kinked domains along which the Pl1b chains are rotated (Figure 4a). These kinked domains show internal strain marked by irregular undulatory extinction. Microprobe analyses show that K-feldspar cores exhibit rather constant composition revealing approximately 10 mol % of albite (Table 2a). Only around enclosed Pl1b chains the alkali feldspar shows a rapid decrease of the albite component (Figure 5).

4.2. Type II: Orthogneiss With Quartz Augens

[13] This rock is characterized by the presence of isolated and elongated quartz augens surrounded by highly elongated K-feldspar and plagioclase polycrystalline aggregates forming almost monomineralic layers (Figure 6). Biotite and muscovite are forming elongated monomineralic aggregates located at boundaries between feldspars and quartz or within plagioclase layers. Quartz augens are composed of grains 150–1000 μm in size with serrated boundaries. Plagioclase (Pl1) polycrystalline aggregates are composed of oligoclase An_{10-20} subequant grains (50–150 μm in

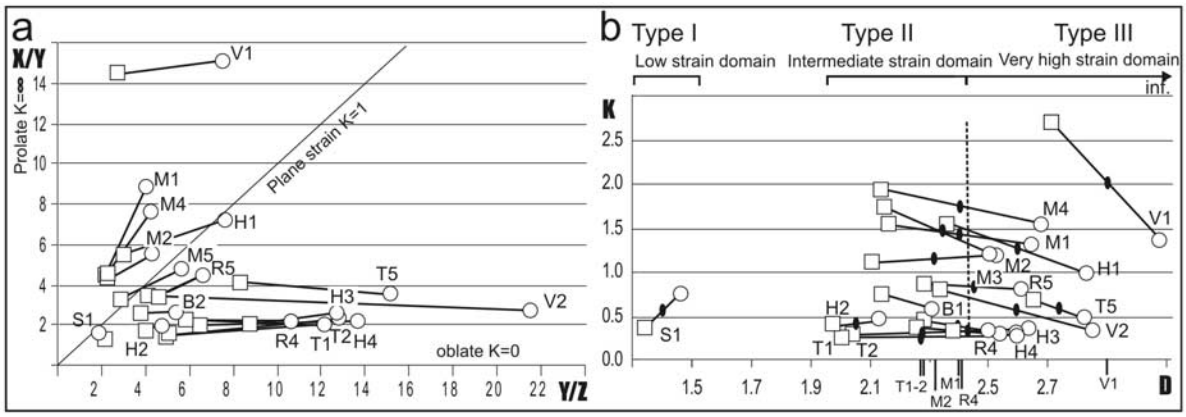

Figure 3. (a) Flinn diagram after *Ramsay and Huber* [1983] shows the shapes of deformation ellipsoids represented as projections of X/Y axial ratios on the ordinate and Y/Z ratios on the abscissa in the graph. This diagram allows to visualize the shapes of the strain ellipsoid and the intensity of deformation in the 2-D diagram. (b) Diagram showing strain intensity expressed as the D parameter on the abscissa against shape K parameter on the ordinate; K = (X/Y-1)/(Y/Z-1) varies from 0 for oblate shapes, to 1 for plane strain shapes, and to infinity for prolate shapes, $D = (((X/Y-1)^2 + ((Y/Z-1)^2)^{1/2}$. The values are obtained by measuring 30 ellipses (harmonic sum) from XZ and YZ sections (principal planes of finite strain ellipsoid). Squares show quartz, and circles show undifferentiated feldspar. Rock types are determined according to the bulk strain intensity and macroscopic appearance (Figure 2) from weakly deformed metagranite S1; intermediate strained augen orthogneiss samples T1, T2, M2, M1, and R4; and highly strained banded orthogneiss samples H1, T5, V1, and V2.

Table 2a. K-Feldspar Compositions[a]

Sample	S1	S1	M1	M1	V1	V1
Analysis	50	48	71	79	92	104
SiO_2	65, 27	64, 07	64, 09	65, 05	64, 63	64, 96
Al_2O_3	18, 69	18, 42	18, 22	18, 56	18, 73	18, 71
CaO	0, 00	0, 03	0, 04	0, 00	0, 03	0, 04
Na_2O	1, 20	0, 49	0, 29	1, 37	1, 10	0, 59
K_2O	15, 87	16, 46	16, 86	15, 52	15, 90	16, 48
Total	101, 04	99, 49	99, 50	100, 54	100, 40	100, 82
Si	2, 986	2, 985	2, 990	2, 988	2, 978	2, 984
Al	1, 008	1, 011	1, 002	1, 005	1, 017	1, 013
Ca	0, 000	0, 002	0, 002	0, 000	0, 002	0, 002
Na	0, 106	0, 044	0, 026	0, 122	0, 098	0, 053
K	0, 926	0, 978	1, 004	0, 910	0, 935	0, 966
Total	5, 026	5, 020	5, 024	5, 024	5, 030	5, 017
X_{Or}	89, 69	95, 53	97, 27	88, 17	90, 36	94, 66
X_{Ab}	10, 31	4, 32	2, 54	11, 83	9, 50	5, 15
X_{An}	0, 00	0, 15	0, 19	0, 00	0, 14	0, 19

[a]Structural formulae calculated on the basis of 8(O).

Table 2c. Large or Interconnected Plagioclase: Pl1 Compositions[a]

Sample	S1	T1	M1	M1	V1
Analysis	43	114	67	91	109
SiO_2	64, 60	64, 70	65, 62	63, 75	65, 55
Al_2O_3	22, 72	22, 84	21, 43	23, 06	22, 22
CaO	3, 48	3, 76	2, 36	4, 38	3, 07
Na_2O	9, 88	10, 03	11, 03	9, 48	10, 23
K_2O	0, 23	0, 13	0, 10	0, 27	0, 22
Total	100, 91	101, 46	100, 56	100, 97	101, 30
Si	2, 827	2, 819	2, 878	2, 797	2, 854
Al	1, 172	1, 173	1, 108	1, 192	1, 140
Ca	0, 163	0, 176	0, 111	0, 206	0, 143
Na	0, 838	0, 847	0, 938	0, 806	0, 864
K	0, 013	0, 007	0, 006	0, 015	0, 012
Total	5, 013	5, 022	5, 040	5, 017	5, 013
X_{Or}	1, 26	0, 70	0, 53	1, 47	1, 20
X_{Ab}	82, 65	82, 26	88, 95	78, 49	84, 75
X_{An}	16, 09	17, 04	10, 52	20, 04	14, 05

[a]Structural formulae calculated on the basis of 8(O).

size) with straight boundaries meeting at triple point junctions (Figures 5 and 6c and Table 2c). Plagioclase polycrystalline aggregates often contain biotite flakes parallel to the foliation or interstitial quartz and new plagioclase An_{1-10} (Pl2). K-feldspar polycrystalline aggregates are composed of slightly elongate to subequant grains with straight boundaries forming a well developed triple point network lined by narrow films of pure albite An_{1-10} (Pl2). Disintegration of the K-feldspar layers into elongate aggregates surrounded by fine-grained Pl1 matrix was observed in some samples. This process is connected to the development of bands filled with recrystallized Pl1 grains up to 150 μm wide oblique with respect to the long axis of the feldspar polycrystalline aggregates (Figure 6b). Finally, elongated thin aggregates of Pl1 are smeared out in the K-feldspar rich matrix. Quartz also forms weakly elongated polymineralic aggregates characterized by highly irregular boundaries with the surrounding feldspar matrix. Common feature are the lobes of quartz and cusps of the K-feldspar pointing in the direction perpendicular to the long face of the aggregate and to the macroscopic foliation.

4.3. Type III: Banded Mylonitic Orthogneiss and Ultramylonite

[14] Banded mylonitic orthogneiss is marked by thin quartz ribbons less than 1000 μm wide. They are surrounded by polymineralic layers of plagioclase, quartz and K-feldspar (Figure 7b). Micas are generally dispersed in the matrix or form narrow layers parallel to the foliation (Figures 7c and 7d). Disintegrated relics of plagioclase aggregates are composed of Pl1 grains An_{14-20} (Figure 5 and Table 2c) and of K-feldspar grains 50–100 μm in size (rarely 200 μm) and of irregular shapes. The interfacial boundaries with K-feldspar are generally straight and commonly lined by rims of Pl2 (An_{4-12}) or thin layers of quartz. Locally, relics of the K-feldspar layers that are a few grains wide ($\sim$250 μm) occur with straight mutual boundaries lined by Pl2 films. The quartz commonly occurs in the form of isolated grains with serrated boundaries and cusps pointing perpendicular and parallel to the macroscopic foliation. However, the most common are few hundred microns wide quartz ribbons composed by elongate, 200–300 μm wide and up to 1000 μm long grains with highly serrated boundaries.

[15] A rather exceptional kind of Type III microstructure is represented by the exceptionally coarse-grained, mylonitic orthogneiss sample B2. This rock type is characterized by polymineralic layers with poorly defined boundaries and a large average grain size of plagioclase and K-feldspar ranging from 160 to 200 μm. The Pl1 grains in relict plagioclase aggregates show sutured boundaries and wide Pl2 rims while the interstitial Pl2 grains in the K-feldspar rich aggregates form wide films and cuspate pools. The interstitial quartz (100 μm in size) occurs in the form of serrated grains in triple point junctions of K-feldspar and Pl1 relict aggregates.

Table 2b. Isolated Plagioclase Pl1b and Pl2 Compositions[a]

Sample	S1	T1	T1	M1	V1
Analysis	52	119	115	77	105
SiO_2	68, 72	69, 06	67, 94	68, 67	67, 69
Al_2O_3	19, 70	19, 74	20, 19	19, 78	20, 69
CaO	0, 31	0, 10	0, 78	0, 22	1, 28
Na_2O	11, 84	12, 14	11, 27	11, 77	11, 19
K_2O	0, 05	0, 12	0, 12	0, 54	0, 23
Total	100, 62	101, 19	100, 30	101, 01	101, 09
Si	2, 986	2, 986	2, 963	2, 980	2, 938
Al	1, 009	1, 006	1, 038	1, 012	1, 058
Ca	0, 014	0, 005	0, 037	0, 010	0, 060
Na	0, 998	1, 018	0, 953	0, 991	0, 942
K	0, 003	0, 007	0, 007	0, 030	0, 013
Total	5, 010	5, 022	4, 998	5, 023	5, 010
X_{Or}	0, 28	0, 64	0, 67	2, 90	1, 26
X_{Ab}	98, 30	98, 91	95, 67	96, 11	92, 87
X_{An}	1, 42	0, 45	3, 66	0, 99	5, 87

[a]Structural formulae calculated on the basis of 8(O).

4.4. Topology of Interstitial Phases in Plagioclase and K-Feldspar Aggregates

[16] The most common interstitial phase at the grain scale are thin films of Pl2 and quartz up to 50 μm long and 10 μm wide located along the mutual plagioclase boundaries, often at high angle to the foliation or in the form of cuspate pools at triple point junctions. The mutual boundaries of Pl1 aggregate grains are often lined by narrow rims of new plagioclase An_{1-10} (Pl2). In Type II orthogneiss samples showing strongly elongated recrystallized K-feldspar and Pl1 grains (samples T1, T2), the Pl2 films exhibit preferred orientation parallel to the direction of maximum stretching, i.e., along the crystal faces parallel to the foliation (Figure 8). In the M1, M2 samples of the orthogneiss Type II, the shape preferred orientation of the recrystallized feldspar is low,

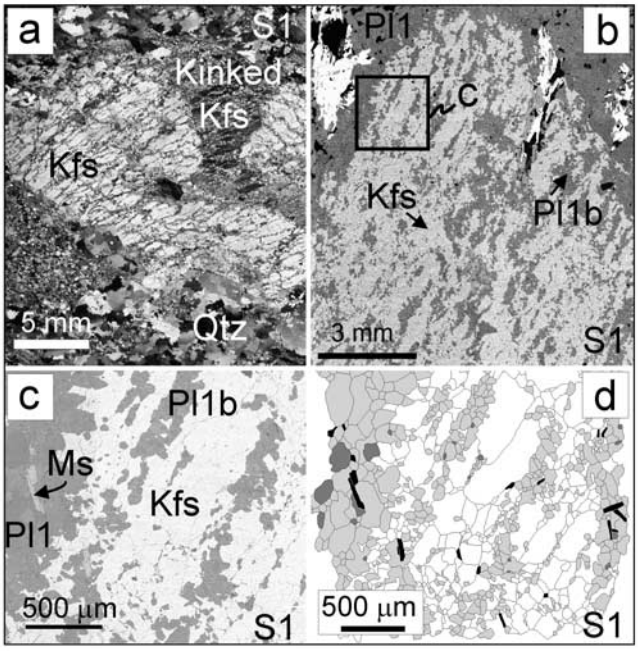

Figure 4. Type I microstructure (S1 sample). (a) Type I metagranite marked by large alkaline feldspar clasts decomposed into albite chains and K-feldspar and (b) scanning electron microscope (SEM) image of alkaline feldspar decomposition. Rectangle indicates the position of the detailed SEM image. (c) The detail of the SEM image showing the shapes of new bulbous albite grains. (d) Corresponding ArcView Geographical Information Systems (GIS) image used for the quantitative mirostructural analysis. Scanning electron microscope images obtained in backscattered electron mode (Camscan microscope, Institute of Petrology and Structural Geology Prague). K-feldspar is represented in light gray, biotite is represented as white laths, quartz and plagioclase are shown in dark gray, and rectangular white mica laths are shown in light gray. In ArcView GIS images the K-feldspar is represented in white, white mica and biotite are represented in black, plagioclase is represented in light gray, and quartz is represented in dark gray. The ArcView Geographical Information System was used as an ideal environment for digitizing mineral shapes [*Lexa et al.*, 2005]. Mineral abbreviations correspond to those of *Kretz* [1983].

which corroborates the development of thin albite-quartz films along the feldspar faces oriented along two maxima with respect to the macroscopic layering (Figure 8). The mean orientation of the Pl2 and quartz seams form an angle of 10–15° with respect to the foliation trace. Interstitial convex quartz grains often occur at triple point junctions but locally line the feldspar boundaries as narrow films (Figures 6c and 6d).

[17] The presence of interstitial phases is the most pronounced in Type III orthogneiss (samples R3, V1 and B2 in particular) where the recrystallized feldspar grains exhibit no shape preferred orientation. Here, wider cuspate-lobate pools and narrow films of Pl2 and quartz occur at a high angle to the macroscopic foliation. The B2 sample shows an extreme orientation of Pl2 seams which form an angle of up to 70° with the foliation trace.

[18] Another important feature is the development of intragranular, wedge shaped fractures that are predominantly developed in elongated feldspar grains with stronger SPO in samples T1 and T2 (Figure 8). These gently curved fractures often originate at the foliation-parallel grain boundaries or triple point junctions, terminate in the interior of the grains and are oriented at low angles (15–30°) to the maximum stretching. In Type III orthogneiss samples (e.g., sample B2) the intragranular fractures occur as well being oriented at high angle to the principal stretching direction.

5. Quantitative Textural Analysis

[19] The quantitative analysis of grain shapes and boundaries was carried out in an ArcView GIS environment. Examples of analyzed samples are shown in Figures 4d, 6d, and 7d. The statistical parameters involving grains size distributions, shape preferred orientation, degree of grain elongation and grain contact frequencies were performed using the MATLAB PolyLX toolbox [*Lexa et al.*, 2005] in order to quantify the above described microstructural sequence of rock types. The grain size distribution was evaluated as an important parameter in deformed rocks because of its sensitivity to stress and temperature [*Schmid et al.*, 1999]. The correct determination of grain size is essential in polyphase systems, where stress and strain rate partitioning are expected [*Handy*, 1990]. Another important parameter is the shape of recrystallized grains, which is strongly dependent on the type of deformation mechanisms and grain growth history [*Boullier and Guéguen*, 1975; *Schmid et al.*, 1987]. Grain contact distribution in the rock yields information about the evolution of spatial distribution of the different minerals in rocks with deformation or melting [*Lexa et al.*, 2005; *Hasalová et al.*, 2008]. This is expressed by the grain contact frequency (GCF) that statistically quantifies the deviation of the grain contact distribution from random [*Kretz*, 1969]. The aggregate distribution, marked by the dominant presence of like-like contacts, represents one end-member of the spatial distribution of grain boundaries that is resulting from the solid state differentiation process [*McLellan*, 1983]. The regular distribution is characterized by the predominance of unlike contacts in rock and is considered as a second end-member

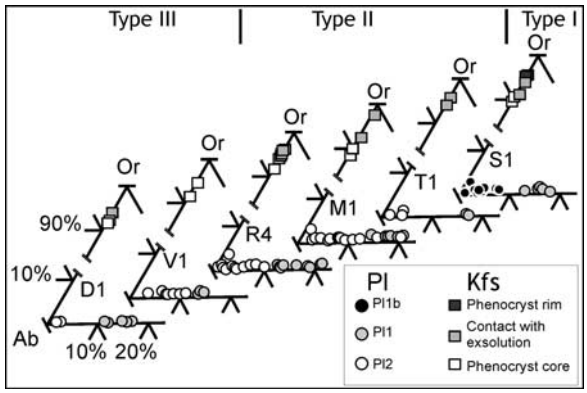

Figure 5. Ternary diagrams showing the composition of feldspars in different samples. Pl1 corresponds to isolated plagioclase aggregate (see text for explanation).

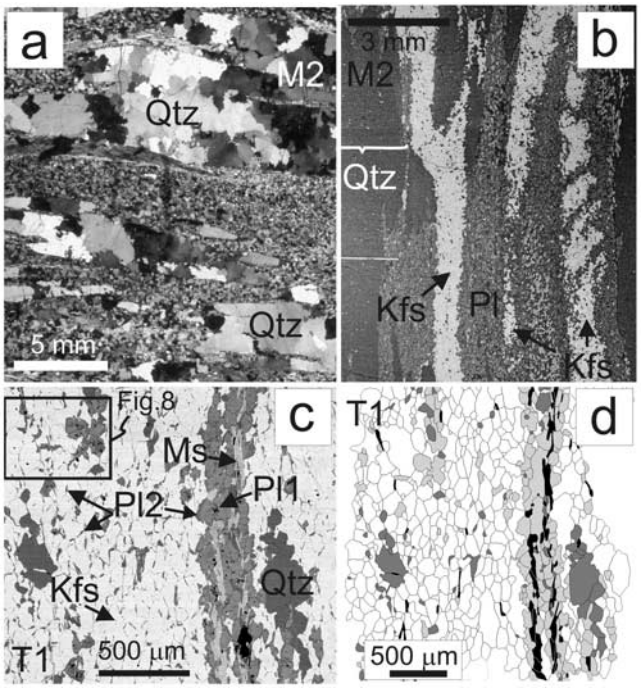

Figure 6. Type II microstructure. (a) Micrograph of sample M2 Type II microstructure characterized by large quartz ribbons and fine-grained feldspar matrix, (b) SEM image of the M2 sample showing typical monominerallic layering and plagioclase aggregate bridges, and (c) detailed SEM image of the T1 sample showing K-feldspar and plagioclase polycrystalline aggregate microstructure. The characteristic feature is the high elongation of feldspar grains lined with Pl2 films, (d) corresponding ArcView GIS drawing of Type II microstructure of the T1 sample. The SEM and ArcView GIS colors are the same as in Figure 4.

of the spatial distribution of the grain boundaries that develops mostly because of solid state annealing [*Flinn*, 1969], mechanical mixing [*Kruse and Stünitz*, 1999] or crystallization of the interstitial melt [*Dallain et al.*, 1999; *Hasalová et al.*, 2008].

5.1. Crystal Size Distribution

[20] The grain size distributions of recrystallized quartz, K-feldspar and of plagioclase have been determined on the basis of more than 500 measured grains per thin section for each sample (except of about 200 measurements in coarse-grained sample B2). Because of the ubiquitous lognormal distribution of the grain populations, the median value was considered to be the most reliable statistical value and the spread of the grain size distribution was evaluated as a difference between the third and first quartile instead of the standard deviation.

[21] The K-feldspar shows a similar grain size distribution for all rock types and is characterized by the median grain size ranging from 60 to 180 μm (Figure 9a). Except sample B2 with exceptionally large grain size, the grain size spread does not follow any systematic pattern. However, the interstitial quartz shows an increasing median grain size value from 20 to 50 μm in the Type II orthogneiss to 80–100 μm in Type III orthogneiss. The plagioclase was examined for the interstitial and aggregate positions separately. The most striking feature is a progressive increase of the aggregate plagioclase grain size from 60 μm (median value) in metagranite to 90 μm in augen orthogneiss to 110 μm in banded orthogneiss, and to 170 μm for sample B2 (Figure 9a). We also observe a systematically higher grain size of aggregate grains compared to the interstitial plagioclase grains for all rock types. In addition, the median value of the aggregate plagioclase grains is shifted toward the third quartile value, while in the interstitial grains it is closer to the first quartile value.

[22] In order to obtain information about the crystal nucleation and growth, the crystal size distribution (CSD) method was applied in the studied samples. The theory of CSD is a well-established technique in metallurgy, ceramics and chemical engineering to reveal information about nucleation, growth rates and growth times of crystals [*Randolph and Larson*, 1971]. CSD in many metamorphic and igneous rocks show a log linear relationship between the grain size L and the population density N according to the equation

$$N = N_0 e^{-L/Gt}$$

where N_0 and Gt are constants and may be related to the nucleation density and growth rate of the crystals [*Higgins*, 1998]. This technique was previously successfully applied to the metamorphic rocks by *Cashman and Ferry* [1988], *Hasalová et al.* [2008], and *Lexa et al.* [2005]. CSD plots of

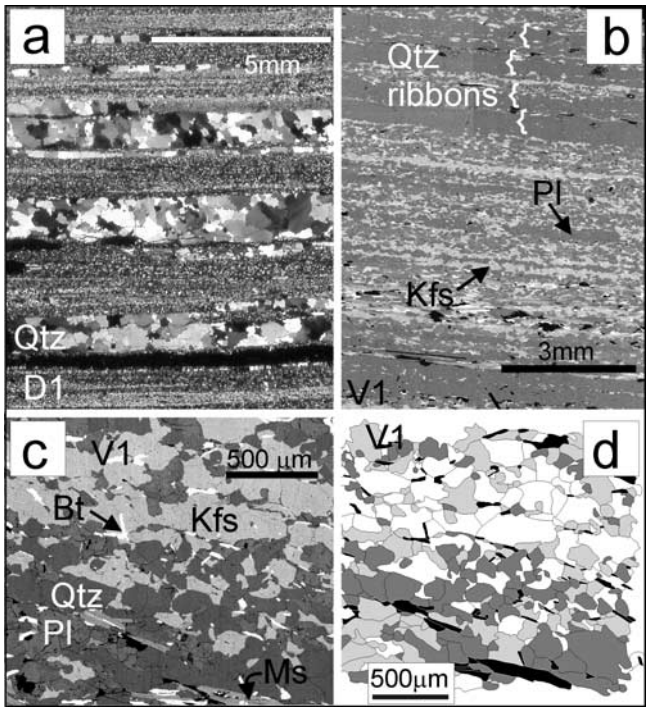

Figure 7. Type III microstructure of banded orthogneiss. (a) Micrograph of sample D1 showing layers of quartz alternating with mixed layers of feldspars and quartz, (b) SEM image of the sample V1 showing quartz and feldspar mixing and poor definition of layer boundaries, (c) detailed SEM image of K-feldspar and plagioclase mixing in the matrix, and (d) corresponding ArcView GIS drawing. The SEM and ArcView GIS colors are the same as in Figure 4.

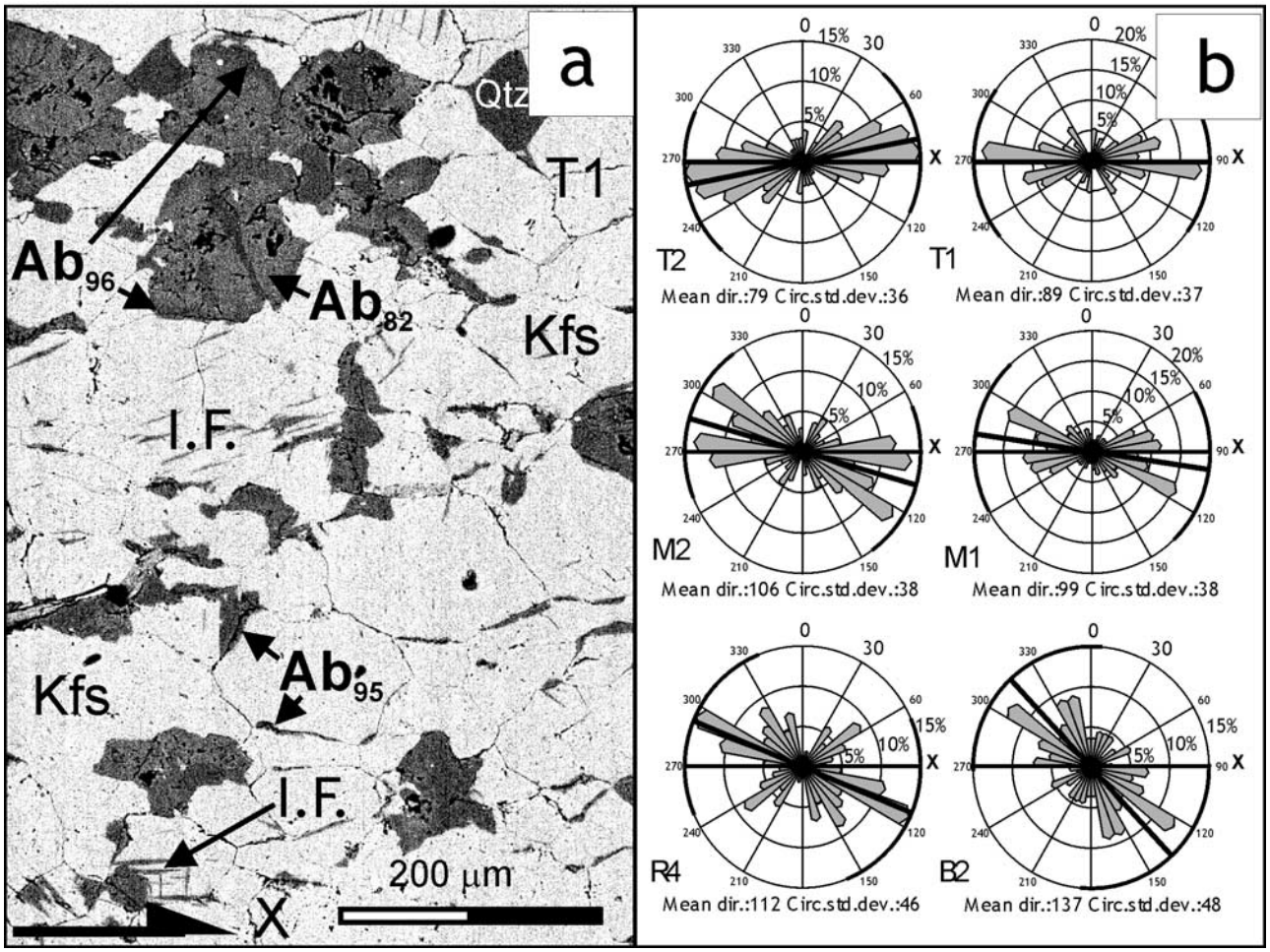

Figure 8. (a) Detail from the backscattered scanning electron image of sample T1 (location of Figure 8a is shown in SEM image in Figure 6c). The image shows the distribution of albite seams along boundaries of K-feldspar grains, character of compositional zoning of the plagioclase in the top left, and intragranular fractures filled with albite (I.F.). (b) Rose diagrams show preferred orientation of ~100 interstitial quartz and Pl2 seams in K-feldspar aggregate. The mean direction and standard circular deviation are shown in the bottom of each diagram. The thick horizontal line represents the orientation of lineation (X), and the thin line shows the orientation of the mean direction.

all the samples constructed according to the method by *Peterson* [1996] exhibit linear correlations between the logarithm of the population density (i.e., the number of crystals per size per volume) and the crystal size (Figure 9b). Applying the theory of CSD, such distributions could be parameterized by the zero size intercept N_0 (nucleation density) and slope Gt (growth rate multiplied by time). These two parameters are plotted in a N_0-Gt diagram [*Lexa et al.*, 2005] where the samples form a distinct trend. Trends in the grain size distributions using CSD method are visualized in Figure 9b. The crystal size distribution plot of the plagioclase aggregates is the most pronounced and shows a systematic decrease of N_0 and an increase of the G_t values with increasing degree of deformation i.e., from Type I to Type III rocks.

5.2. Grain Shapes and Shape Preferred Orientation (SPO)

[23] The aspect ratio median value of plagioclase and K-feldspar varies between 1.5 to 3.1 and no systematic pattern related to the type of rocks and the degree of deformation is obvious (Figure 10). However, the SPO of plagioclase and K-feldspar in most of Type II and III orthogneiss samples is higher compared to the Type I sample with exceptionally high SPO for samples T1 and T2. There is a difference between the aggregate plagioclase (Pl1) and the interstitial albite (Pl2) marked by a systematically higher SPO for the former compared to the latter.

5.3. Grain Contact Frequencies (GCF) and Grain Boundary Preferred Orientation (GBPO)

[24] The combination of the GCF analysis with the studies of the preferred orientation of the like-like (like–like contacts = boundaries of minerals of the same species) and unlike grain boundaries (GBPO) yields important information about the organization of the grain boundaries with respect to the deformation processes [*Lexa et al.*, 2005]. So far the degree of deviation of the grain boundary distributions from the random distribution has been evaluated by plotting the observed/expected ratio of the like–like

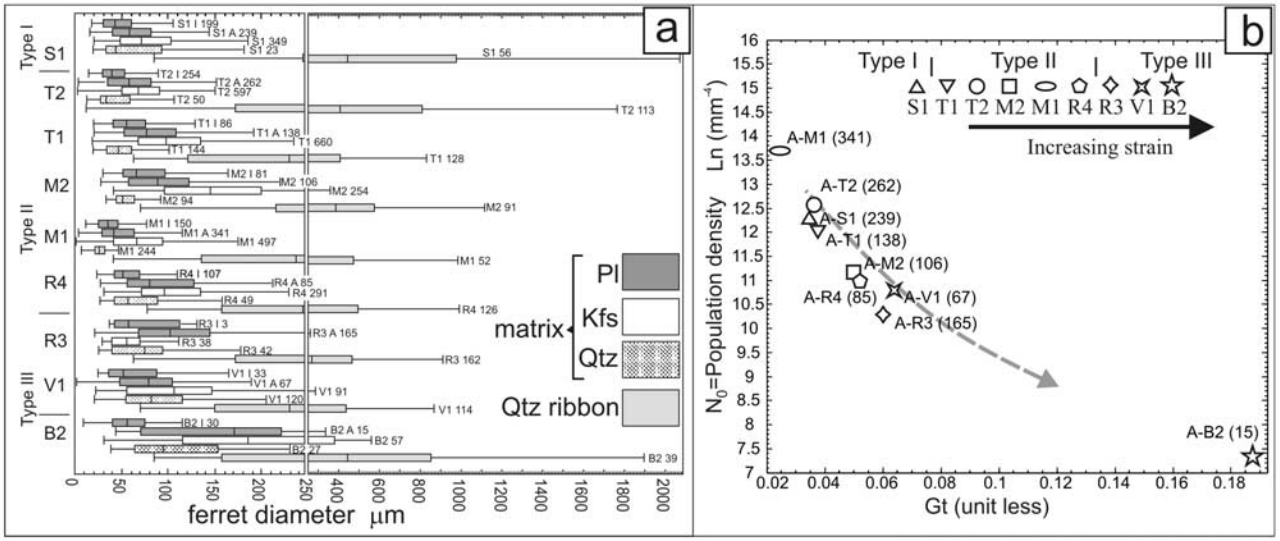

Figure 9. (a) Grain size statistics for the studied samples presented in box-and-whiskers diagrams. Horizontal axis corresponds to the ferret diameter of grain size in micrometers, and the thick bar represents the median of grain size distribution. Vertical axis shows samples arranged according to the degree of deformation from least deformed S1 to most intensely deformed sample V1. B2 represents an exceptionally coarse-grained mylonitic banded orthogneiss. For each sample the plagioclase grain size statistics for interstitial phases (I = Pl2 grains), and for recrystallized grains forming aggregates (A = Pl1 grains) are shown. The number of grains is indicated. Grain size distributions of isolated quartz in the matrix and quartz grains forming centimetric ribbons or augen are also differentiated. This diagram shows progressive coarsening of both Pl1 (aggregate) and Pl2 (interstitial) grains. (b) Plot of crystal size distribution (CSD) for plagioclases (I = Pl2 interstitial grain, A = Pl1 recrystallized grains in aggregates). N_0 ln(mm^{-4}) values on vertical axis represent density of grains per volume, and dimensionless Gt values reflect the grain size frequency distribution. This diagrams show decrease of N_0 values and increase of Gt values which in classical CSD plots represent decreasing values of the intercept of the CSD curve with vertical axis associated with decreasing slope [*Higgins*, 1998]. In the CSD theory this evolution means decreasing nucleation rate and increasing growth rate contribution to the shape of the grain size frequency histogram [*Lexa et al.*, 2005].

contacts of the two major minerals against each other [e.g., *McLellan*, 1983]. *Lexa et al.* [2005] proposed a new diagram where the χ value

$$\chi = \frac{Observed - Expected}{\sqrt{Expected}}$$

is plotted against the ratio of orientation tensor eigenvalues that represent the degree of GBPO. If the solidified melt is identified in a rock the GBPO may yield information about the types of channel networks as defined by *Sawyer* [2001] and quantified by *Hasalová et al.* [2008] and *Závada et al.* [2007].

[25] In this work we use a method proposed by *Lexa et al.* [2005] where the grain contact frequencies are used to assess the character of the spatial distributions of grain boundaries. Figure 11a shows that the plagioclase like-like contacts for the Type I metagranite plots in an intermediate part of the diagram and is characterized by a rather small aggregate distribution. This is due to the presence of the two plagioclase populations resulting from the recrystallization of the large plagioclase crystals (high aggregate distribution) and from the disintegration of the large alkaline feldspar crystals into a mixture of albite and K-feldspar (Figure 4). With increasing deformation a clear evolution of the grain contact frequency toward strongly aggregated distribution for weakly deformed samples of the Type II microstructure can be observed. This is probably due to the coalescence of feldspar and plagioclase layers. At very high strain intensities the plagioclase grain contact frequencies evolve toward the random or regular types of distribution in Type III microstructure. This type of evolution indicates an almost perfect mixing of the plagioclase with other mineral phases. The degree of GBPO of the like-like boundaries for plagioclase does not evolve with the above described trend but remains rather constant for any degree of the finite strain. The K-feldspar grain contact frequency shows a similar behavior to the plagioclase but for some samples a rather strong GBPO coupled with a decreasing grain contact frequency was observed. The evolution of the unlike plagioclase-K-feldspar grain boundaries exactly mirrors the evolution of the plagioclase like-like contact frequency behavior (Figure 11b). For the observed constant grain size it is a geometrical necessity that an increase of the like-like contacts causes a corresponding decrease of the unlike contacts of feldspars.

6. Crystallographic Preferred Orientation

[26] The lattice-preferred orientation (LPO) of quartz, plagioclase and K-feldspar was determined using the electron backscatter diffraction (EBSD) technique [*Bascou et*

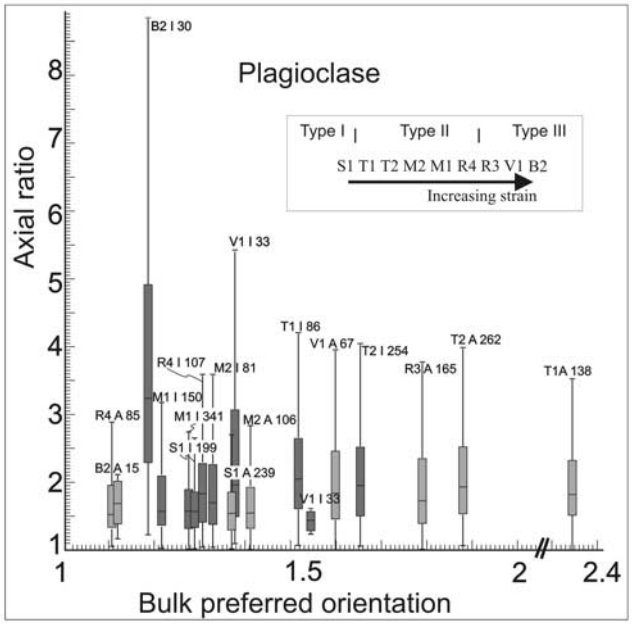

Figure 10. Plot of the grain shape preferred orientations (SPO) of plagioclase and K-feldspar in studied samples. The results are summarized by a box-type plot of axial ratios versus eigenvalue ratios of bulk shape preferred orientation for individual phases. Individual boxes show median and first and third quartile values. The whiskers represent a statistical estimate of the range of data, while outliers are not shown. Vertical axis characterizes the shape of grains, while horizontal axis represents the area-weighted degree of preferred orientation. Plagioclase (I = interstitial Pl2 grains, A = recrystallized Pl1 grains forming aggregates). This diagram shows generally low aspect ratios of plagioclase grains for all samples and exceptionally strong SPO of some samples of Type II and III microstructures.

al., 2001]. The lattice preferred orientation of quartz is presented in the pole figures of the crystallographic directions < c > and < a > (Figure 12). In the case of plagioclase and K-feldspar, the list of operative slip systems [*Kruse et al.*, 2001; *Tullis*, 1983] has been used and measured data has been plotted in the pole figures of these crystallographic planes and directions. Pole figures of principal slip directions and slip planes showing the best coincidence with the main axes of the finite strain ellipsoid of every sample are presented (Figure 13). In the assessment of the maxima position in the pole figures, it has been taken into account that samples M1, V1 reveal prolate shapes of the strain ellipsoid. Hence the maxima of poles in the slip planes might occur along a girdle perpendicular to the slip direction.

6.1. Quartz Augens and Ribbons Crystallographic Preferred Orientation (CPO)

[27] The quartz c axis fabric for Type I microstructure (sample S1) shows a strong central maximum and weaker submaxima close to the periphery of the diagram suggesting an ill-defined oblique cross girdle pattern with opening angles of around 45° (Figure 12). The fabric is a result of the dominant prism < a > and subordinate basal < a > slip systems and a plane strain noncoaxial deformation. Type II microstructures (samples T2 and M1) show strong, central c axis maxima. There is also a tendency to form a single girdle of c axes distribution oriented oblique to the foliation (T2). This c axis pattern is commonly interpreted as a result of a prism < a > slip activity and a noncoaxial deformation [*Schmid and Casey*, 1986]. The Type III microstructure (samples R3 and V1) is characterized by maxima located either at the periphery of the diagram or in an intermediate position. The maxima are organized either along single girdles oblique to the foliation (sample R3) or symmetrically in case of sample V1. These c axis patterns developed from combined activity of the basal < a > and rhomb < a + c > slip systems with a minor contribution of the prism < a > slip during the noncoaxial deformation.

6.2. Plagioclase and K-Feldspar CPO

[28] Plagioclase CPO shows a weakening and an increased activity of secondary and tentative slip systems with microstructural evolution from Type I to Type III microstructures (Figure 13). A frequently described slip system (010)[100] [*Kruhl*, 1996; *Martelat et al.*, 1999; *Schulmann et al.*, 1996] has been observed only in the Type I microstructures (S1) and shows an asymmetry of the position of the maxima with respect to the foliation. The plagioclase from the Type II and III microstructures showed less common slip systems that are supposed to be secondary or tentative [*Kruse et al.*, 2001]. In the Type II microstructure (T2 and M1), the CPO shows active slip systems with dissociated Burgers vectors [*Montardi and Mainprice*, 1987; *Olsen and Kohlstedt*, 1985] namely $1/2[112](11\bar{1})$ and $1/2[111](10\bar{1})$ in the sample T2, and $1/2[1\bar{1}2](110)$ and $1/2[1\bar{1}2](20\bar{1})$ in the sample M1. Brief inspection of both pairs of slip systems shows that each pair occupies a close position in the plagioclase crystal [*Kruse et al.*, 2001, Figure 2] and it is very likely that they operated simultaneously. The Type III microstructures show very weak crystallographic preferred orientation of the plagioclase and sample R3 again reveals an activity on the $1/2[1\bar{1}2](110)$ slip systems with dissociated Burgers vector (Figure 13).

[29] The K-feldspar phenocryst and albite neoblasts of Type I orthogneiss show the same crystallographic orientations (sample S1, Figure 13) that do not coincide with any known slip systems. Albite neoblasts originate along the strings that are parallel to (100) planes. In the Types II and III microstructures, the CPO of K-feldspar recrystallized grains reveal similar pattern indicative of the slip direction parallel to the 1/2[110] in all samples that operate on the (001), $(1\bar{1}1)$ slip planes (Figure 13). A less pronounced slip system $[101](10\bar{1})$ has been recognized in the augen gneiss sample T2 from the Type II microstructure.

7. Petrological Modeling

[30] The structural position and shapes of interstitial phases, the character of mineral zoning and the compositional variations of the plagioclase (Pl2) in both Type II and III microstructures indicate the presence of some kind of fluid during the deformation [*Fitz Gerald and Stünitz*, 1993; *Sawyer*, 2001; *Hasalová et al.*, 2008; *Závada et al.*, 2007]. Therefore, the pseudosection modeling was performed in order to examine whether the deformation process in the studied orthogneisses occurred in the presence of a melt or an aqueous fluid.

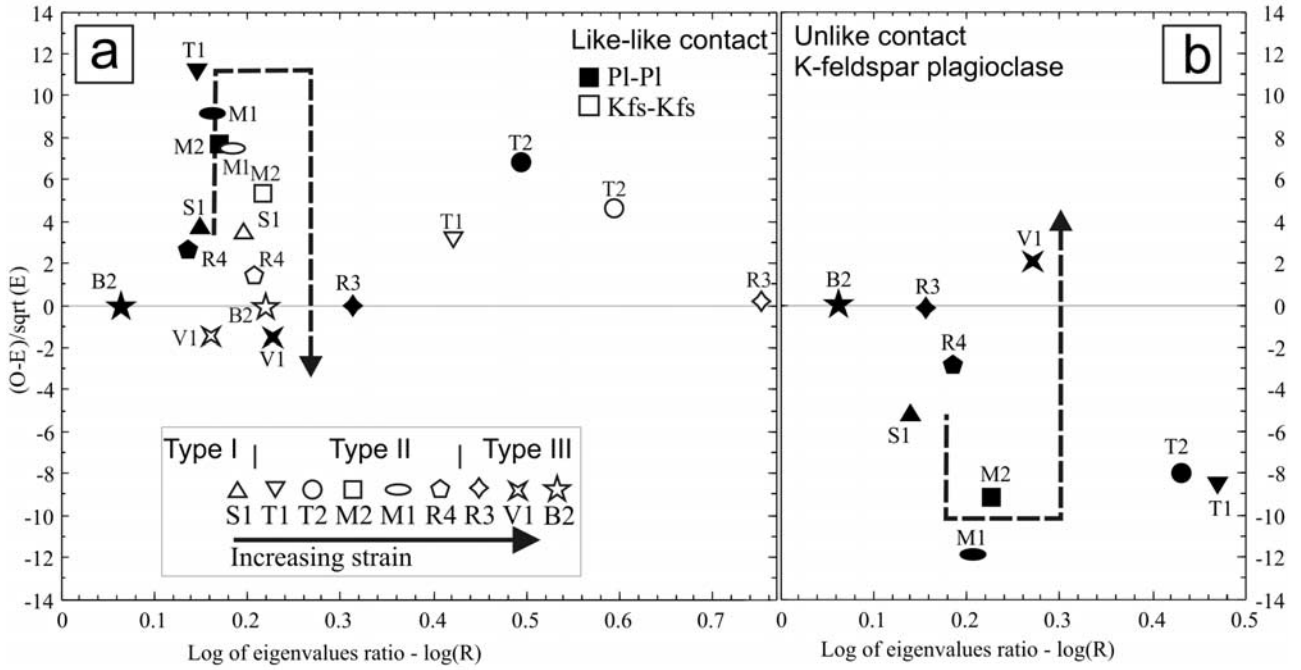

Figure 11. Plot of the grain boundary frequencies. Plots of the deviations from random spatial distribution versus the degree of grain boundary preferred orientation. The value of the deviation from random spatial distribution is obtained by the contact frequency method [*Kretz*, 1969], and the length-weighted degree of preferred orientation is estimated as the ratio of eigenvalues of the bulk matrix of inertia. The plot of the like-like and unlike boundaries is separated. (a) The diagram of feldspars like-like boundaries shows a trend from the weak aggregate distribution of Type 1 microstructure, to the highly aggregate distribution in Type II microstructures, and almost random distribution in highly mixed Type III microstructures. (b) The diagram of feldspar unlike boundaries mirrors the like-like evolutionary trend.

7.1. Modeling Method

[31] The pseudosections were calculated in the system Na_2O-CaO-K_2O-FeO-MgO-Al_2O_3-SiO_2-H_2O (NCKFMASH). All the Fe was treated as FeO and molar amounts of the considered oxides were recalculated to 100 mol %. The calculations were performed using THERMOCALC 3.25 [*Powell et al.*, 1998] and the data set 5.5 [*Holland and Powell*, 1998]. The mixing models for the most solid solutions were taken from *White et al.* [2001] and the THERMOCALC documentation [*Powell and Holland*, 2004]. The feldspars are formulated using the model of *Holland and Powell* [2003], the paragonite-muscovite solution is after *Coggon and Holland* [2002]. The quartz, K-feldspar and plagioclase are in excess and the pseudosections are contoured for liquid mole isopleths.

7.2. Results

[32] The first pseudosection is calculated with the amount of H_2O, $M(H_2O)$ = 2.68 mol % in the whole rock composition, which is the amount of H_2O tied in micas in the assemblage biotite-muscovite-plagioclase-K-feldspar-quartz (Bt-Ms-Pl-Kfs-Qtz) at 8 kbar and 600°C (Figure 14a). The limiting maximum pressure for the studied rock with the assemblage Bt-Ms-Pl-Kfs-Qtz is the appearance of garnet at 8–9 kbar, the maximum temperature limit is the beginning of biotite dehydration melting marked by the appearance of garnet at temperatures of 680–700°C and the breakdown of muscovite at 680–700°C below 6 kbar that is not observed. The minimum pressure and temperature conditions cannot be determined from the assemblage of the studied sample, therefore, we used the P-T path of *Pitra and Guiraud* [1996] that was determined in the neighboring metapelites. It is characterized by decompression from 8–9 kbar and 610–660°C to 4–5 kbar and 600–650°C. Path 1 (Figure 14a) is characterized first by heating followed by decompression. Melting in the assemblage Bt-Ms-Pl-Kfs-Qtz without external H_2O starts at c. 660°C and 8 kbars and the maximum amount of melt produced in the field of Bt-Ms-Pl-Kfs-Qtz-Liq is less then 1 mol %.

[33] The evolution of assemblages that the rock composition produces with a varying amount of H_2O ($M(H_2O)$ = 0–4.78 mol %) on heating at 8 kbar is examined in Figure 14b. The evolution for the amount of H_2O tied in micas (=2.68 mol %) in a rock with the starting assemblage Bt-Ms-Pl-Kfs-Qtz is indicated by path 1, and is equivalent to the isobaric heating path in Figure 14a. The assemblage Bt-Ms-Pl-Kfs-Qtz starts to melt at c. 660°C, and produces less then 0.5% of melt at c. 685°C (path 1 in Figure 14b). The upper temperature limit is the appearance of garnet at c. 690°C that is not observed in the studied rocks. The lower amount of H_2O in the rock stabilizes the anhydrous phases such as the garnet or kyanite and higher amounts of H_2O indicates the presence of free aqueous fluid below 630°C.

[34] If above the temperature of c. 630°C appears free H_2O in the rock that follows the path 1, the rock composition is immediately drawn to the right side, and starts to

melt (for example path 2 in Figure 14a). This leucocratic melt is generated by the water released by the dehydration process in which water migrates upward into the melt-fertile rocks that are above the wet-solidus temperature [*Scaillet et al.*, 1990; *Thompson and Connolly*, 1995]. The quantity of produced melt depends on the amount of available external H_2O. For example the total amount of H_2O for path 2 is $M(H_2O)$ = 4.28 mol %, which is 1.60 mol % of H_2O added to 2.68 mol % H_2O already present in the micas. Such H_2O addition results in the production of 5 mol % of melt at 660°C and 8 kbar.

[35] The evolution during decompression was also studied in P-$M(H_2O)$ sections at 660°C. Following a decompression from 8 to 4.5 kbar, the rock with the original H_2O tied in micas increases the amount of melt to 1 mol %. In a rock that contains added H_2O, the melt fraction increases by 1–2.5%, for example for path 2 the total amount of melt at 4.5 kbar is 7.5 mol % because of 1.6 mol % added H_2O on the prograde path.

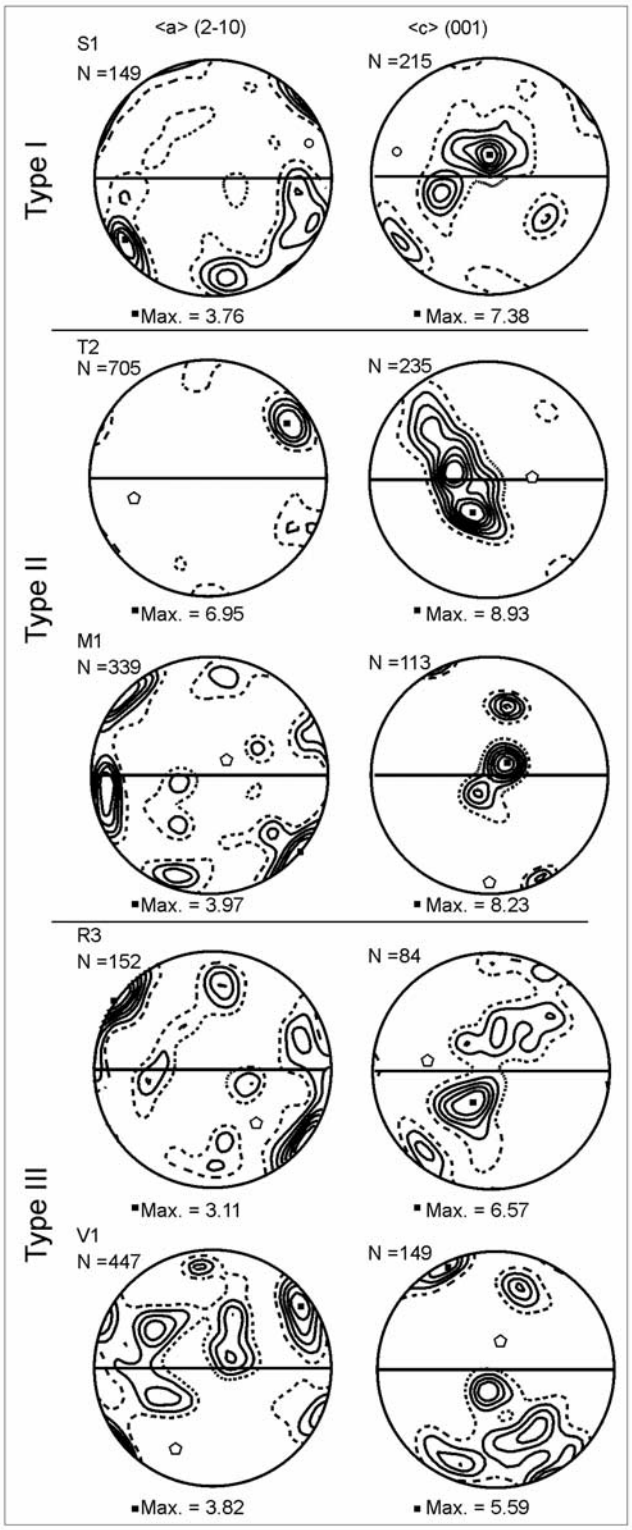

Figure 12. Electron backscatter diffraction in situ measurements on quartz ribbons. Pole diagrams showing contoured crystallographic orientation (projected in lower hemisphere equal area). Contoured at multiples of uniform distribution (maximum 10 uniform). The foliation normal is N-S, and the stretching lineation is E-W. Black squares correspond to the pole of the mean orientation. The pole figures show evolution of active slip systems with increasing deformation from activity of combined prism < a > and basal < a > slip systems for weakly deformed Type I microstructures, via the activity of prism < a > slip system in intermediate Type II microstructures to combined activity of basal < a > and rhomb < a + c > slip systems in highly strained Type III microstructures.

8. Discussion

[36] Here we discuss the anomalously weak K-feldspar and plagioclase compared to quartz in light of the strain data and quantitative microstructural and textural analysis. The quartz-feldspar rheology inversion is discussed as a result of the alkaline feldspar breakdown and the formation of a fine-grained feldspar matrix. Finally, we propose a model of mixing of the recrystallized plagioclase and K-feldspar grains with the silicate melt associated with grain boundary sliding controlled diffusion creep followed by a granular flow at higher melt proportions.

8.1. Comparative Quartz and K-Feldspar Rheology

[37] On the basis of the number of experimental data, the quartz can be considered to be significantly weaker compared to the K-feldspar and plagioclase for a wide range of temperatures [*Jaoul et al.*, 1984; *Kronenberg and Tullis*, 1984; *Tullis*, 1990]. This is supported by a number of studies of quartzo-feldspathic rocks deformed at medium- to high-temperature conditions [*Gapais*, 1989; *Handy*, 1994a; *Schulmann et al.*, 1996]. It is only at greenschist facies conditions and in the presence of hydrous fluids, when feldspars become weaker than quartz via destabilization and breakdown to mixture of retrograde fine-grained reaction products as white mica, quartz (K-feldspar breakdown) and epidote, albite ± garnet (plagioclase breakdown) [*Fitz Gerald and Stünitz*, 1993; *Handy*, 1990; *Stünitz and Fitz Gerald*, 1993]. Nevertheless, it is assumed that the strength of feldspars is generally several orders of magnitude higher than that of quartz [*Handy*, 1994a; *Handy et al.*, 1999; *Ranalli and Murphy*, 1987].

[38] The shapes of quartz and feldspar polycrystalline aggregates measured in this work clearly show that for

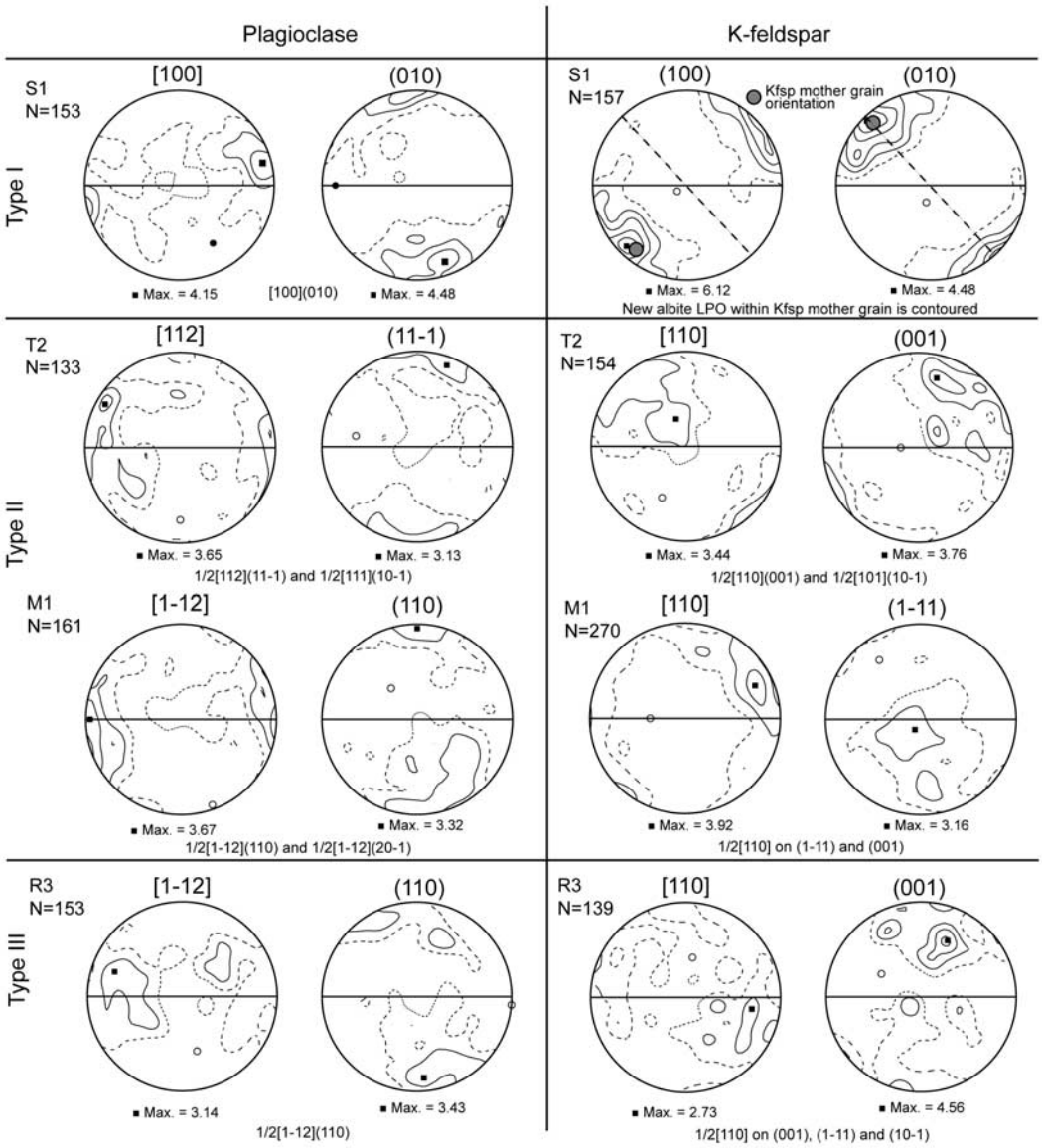

Figure 13. Contoured pole figures of the most characteristic slip direction and slip plane of K-feldspar and plagioclase from the Type I to the Type III microstructures. Equal area projection, lower hemisphere. Contoured at interval 1.0 times of the uniform distribution. Foliation (full line) is horizontal, and lineation is in this plane in the E-W direction. N is the number of measured grains. Maximum densities (black square in the pole figures) are marked below the pole figure. Plagioclase shows commonly reported slip system only for Type I microstructure and activity of secondary and tentative slip systems with dissociated Burgers vectors for Type II and III microstructures. The top right pole figures show dependency of CPO of the new exsolved albite grains Pl1b on the orientation of alkali feldspar host. K-feldspar reveals also slip systems with dissociated Burgers vectors for Types II and III microstructures. See text for discussion.

various deformation intensities the quartz aggregates are less deformed than the feldspar aggregates and the difference of D values between feldspar and quartz aggregates increases with increasing bulk deformation. We suggest that the studied samples reveal a higher competency of quartz compared to the feldspar polycrystalline aggregates for all examined strain intensities at high-temperature conditions. The strength reversal between the quartz and feldspar in experimentally deformed aplite was documented by *Dell'Angelo and Tullis* [1996]. These authors showed that at 700°C, the dispersed quartz grains in the aplite remain less deformed than the feldspar grains while at higher temperatures the interconnected quartz becomes weaker than feldspars.

8.2. Structural Evolutionary Trends of Polyphase Mylonites

[39] We discuss here a hypothesis of microstructural evolutionary trend in which the Types I, II and III microstructures represent different deformation stages along a

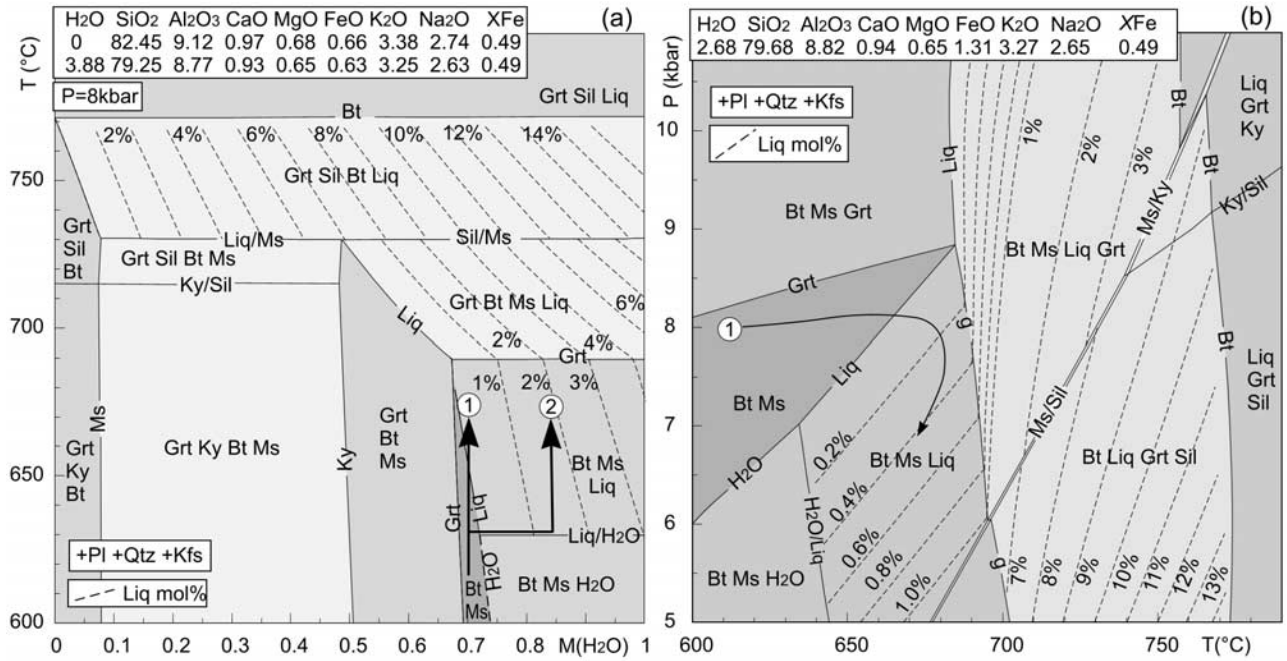

Figure 14. (a) Pseudosection showing the evolution of assemblages that the rock composition produces with varying amounts of H_2O (M(H_2O) = 0–3.88 mol %) on heating at 8 kbar. (b) The pseudosection calculated with the amount of H_2O tied in micas, deduced from pseudosection (Figure 14a). The pseudosection shows a prograde path between 7 and 8 kbar along which the melt appears above 640°C in the stability of Bt-Ms-Liq-Pl-Ksp-Qtz. For comparison, the contours of melt production in other fields are also shown. Mineral abbreviations correspond to those of *Kretz* [1983].

progressive deformation path. Theoretically, the load-bearing framework (LBF) minerals (LBF = interconnected strong phase) should shield a weak phase from viscous deformation for weak phase fractions lower than 20% [*Handy*, 1990]. With increasing strain the weak phase starts to interconnect along localized shear bands, leading finally to the development of a banded structure of alternating monomineralic layers [*Jordan*, 1988]. This corresponds to an evolution from high-viscosity contrast toward low-viscosity contrast interconnected weak layer (IWL) structures [*Handy*, 1994a].

[40] The microstructure of the Type I orthogneisses show interconnected recrystallized aggregates of plagioclase (representing the weakest phase) surrounding strong clasts of quartz and alkali feldspar. This kind of microstructure corresponds to IWL microstructure with the deformation highly localized into rheologically weak plagioclase and a relatively high volume (up to 60 vol. %) of strong fraction (Figure 15a). This observation is valid for the macroscopic scale, but different rheological behavior can be observed at the scale of the individual feldspar clasts. The internal structure of the alkali feldspar phenocrysts shows typical characteristics for a LBF structure formed by K-feldspar and aggregates of recrystallized plagioclase representing an isolated weak phase [*Eudier*, 1962; *Jordan*, 1987; *Tharp*, 1983]. A rather high volume of weak pockets (20–30%) indicates a low stability of the LBF structure for small strain intensities [*Handy*, 1994a]. This is consistent with the observed onset of coalescence of plagioclase chains along microshear bands in Figure 6b [*Jordan*, 1988].

[41] The Type II microstructures are characterized by the collapse of the internal LBF structure of alkali feldspar through the interconnection of recrystallized plagioclase and K-feldspar. This evolution is documented by the presence of oblique ''bridges'' of recrystallized plagioclases crossing recrystallized K-feldspar aggregates and connecting surrounding plagioclase matrix (Figure 6b). From a rheological point of view, the volume of the weak matrix increased from $\sim$ 30 to 60 vol. % through the addition of entirely recrystallized plagioclase and K-feldspar from original phenocrysts of Type I rock to already recrystallized plagioclase of Type II orthogneiss (Figure 15b). This evolution leads to the development of IWL structures at all scales marked by a low volume of strong phases (quartz) and a moderate viscosity contrast indicated by the elongated shapes of quartz aggregates. An important feature of this stage is the coalescence of K-feldspar and plagioclase leading to the development of almost monomineralic layers (Figure 6).

[42] The Type III microstructure is characterized by the destruction of feldspar monomineralic layering through progressive mixing of the feldspars and the subordinate small quartz grains forming a fine-grained matrix. The final microstructure is represented by highly elongated quartz ribbons surrounded by the homogeneously deformed feldspar-quartz matrix. This type of rock microstructure corresponds to the IWL structures and is marked by a very low-viscosity contrast between the quartz and the weak phases. The stronger quartz can be seen as a deformable inclusions in weak matrix (Figure 15c). In order to develop such a microstructure the deformation mechanisms of feldspars have to evolve toward similar efficiency.

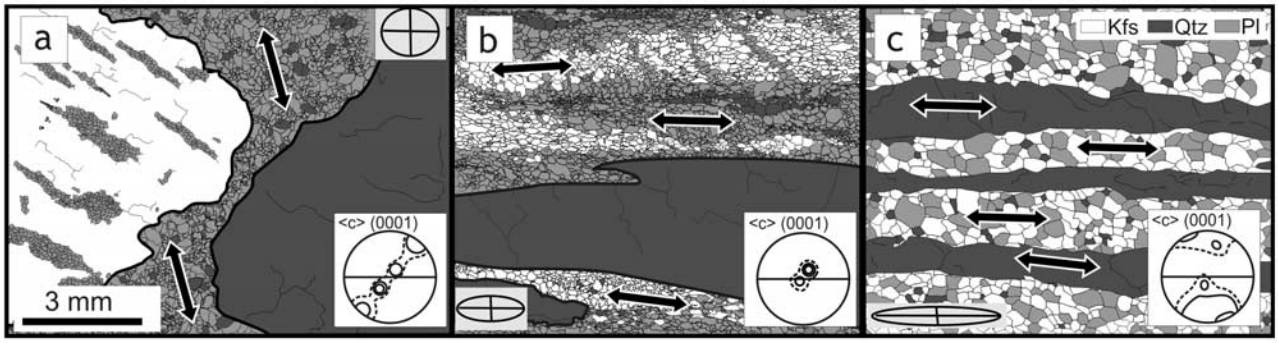

Figure 15. The evolutionary trend of the metagranite deformation. (a) Orthogneiss Type I showing interconnected weak layer (IWL) structure with strain concentration in plagioclase. The K-feldspar shows internal load-bearing framework structure with weak plagioclase strings, while quartz exhibits weak CPO, both indicating shielding of quartz and feldspar from viscous flow. (b) Orthogneiss Type II is marked by almost uniform flow in plagioclase and K-feldspar monomineralic layers around the strong quartz-IWL structure with low viscosity contrast. The rock shows development of monomineralic layering and intense yielding of quartz marked by strong CPO and activity of prism < a > slip. (c) Orthogneiss Type III shows a uniform flow of all mineral phases and mixing of feldspars associated with important crystal growth. The quartz texture exhibits weakening comparing to the previous stage and activity of the basal < a > slip.

8.3. Mechanism of Alkali Feldspar Breakdown: Transition From Type I to II Rock

[43] The key element controlling the rheological development of the bulk rock is the mechanism of decomposition of originally large alkali feldspar phenocrysts into chains of plagioclase grains and adjacent K-feldspar hosts (Figure 4). EBSD measurements have shown that the texture of the new plagioclase crystals in any structural position is almost identical to that of the K-feldspar hosts (Figure 13), indicating an orientation relationship between the host and the inclusion.

[44] The above described features do not have an unambiguous explanation. The coherent texture of the plagioclase and host K-feldspar grain may reflect a heterogeneous nucleation process [*Putnis et al.*, 2003; *Ribbe*, 1983]. The Time-Temperature-Transformation diagrams for the feldspar exsolution during cooling suggest that a process of heterogeneous nucleation is the most likely mechanism because of the slow cooling rates (which are likely to occur in deep seated intrusions) [*Putnis et al.*, 2003]. Our microstructural analyses show that the shape and size of the exsolution patterns is determined by the structure of the host namely by (100) and (010) planes of alkali feldspars. The experiments of *Putnis et al.* [2003] show that the albite rich regions originate as a monoclinic feldspar exsolution in the K-rich host. With falling temperatures the albite changes to a high-albite triclinic structure. The strain generated at the lamella interface leads to the segmentation of the lamella by the albite twinning reducing the strain energy across the interface region. It is possible that such twinned lamellae coarsen during the subsequent annealing which may lead to the development of new albite grains. The process of coarsening may have been enhanced by the thermally induced deformation so that first subgrains and subsequently developed new grains originated from the progressively deforming twinned lamellae. All these processes may result in the development of chains of albite grains subparallel to the former exsolution domains. The process of the heterogeneous nucleation is supported by the compositional profiles which show a decrease of albite components in the host K-feldspar toward the albite boundary of rather constant composition similarly to the profiles published by *Putnis et al.* [2003]. In theory the exsolution process should be related either to the cooling history of crystallization of the granite or to the deformation-metamorphism process as suggested by *White and Mawer* [1986, 1988]. However, the spatial distribution of plagioclase chains in the feldspar host and the crystallographic coherency suggest that the transformation of the original alkali feldspar was achieved by heterogeneous nucleation.

8.4. Consequences of Feldspar Breakdown: Monomineralic Layering in Type II Rocks

[45] The progressive textural evolution toward aggregate distribution in the Type II microstructure is a typical feature of the high-grade deformation of granitoids [*Gapais*, 1989; *Handy*, 1994a; *Schulmann et al.*, 1996]. The onset of granite deformation is marked by the high stress concentrations in the plagioclase grains due to the relative rheological inactivity of the quartz and K-feldspar at the onset of the metagranite deformation (Type I microstructure). The grain size increase of the recrystallized plagioclase and K-feldspar associated with the development of monomineralic layering can be interpreted in terms of stress relaxation [*Hobbs*, 1981] coupled with a flow stress increase in the quartz aggregates indicated by the activity of the prism < a > slip system compared to the basal < a > in the Type I microstructure [*Schmid and Casey*, 1986]. Alternatively, the evolution of the quartz slip system can be attributed to the increasing strain intensity in the Type II microstructure [*Heilbronner and Tullis*, 2006]. Rather unusual feldspar slip systems like once in Type II rocks (Figure 13) have been reported by *Baratoux et al.* [2005] from high-grade mylonitic metagabbros and by *Franěk et al.* [2006] from partially molten granulites. These authors interpreted the observed slip systems as a result of a grain boundary sliding accompanied with a crystal plastic deformation. All this

implies a progressive homogenization of the stress field during this stage. Differences in the efficiency of the deformation mechanisms lead to the development of monomineralic layering precluding effective mechanical mixing. We emphasize that the involvement of feldspars in the homogeneous flow increases the proportion of the weak material up to 60%, which provided a significant drop of the bulk strain rate or stress assuming constant far field stresses or a bulk strain rate, respectively (Figure 15b). The effective weakening mechanism could be regarded in the presence of fluid or melt phase at grain boundaries in Type II rocks which is represented by the interstitial albitic Pl2 and quartz forming thin films parallel to the K-feldspar and Pl1 boundaries or as small cuspate grains in triple point junctions.

8.5. Reasons for Transition From Type II to Type III Rock: Melt-Assisted Mineral Mixing

[46] Type III microstructures correspond to a mixing of fine-grained plagioclase and K-feldspar by two competitive processes: a mechanical mixing accompanied by syn-deformational mass transfer either by diffusion [*Baratoux et al.*, 2005; *Kruse and Stünitz*, 1999] or by melt/fluid redistribution along grain boundaries during the in situ melting [*Závada et al.*, 2007; *Hasalová et al.*, 2008] or infiltration of hydrous fluids, respectively [*Stünitz and Fitz Gerald*, 1993]. The mechanical mixing process is supported by the progressive thinning of the plagioclase aggregates in a K-feldspar matrix associated with the extreme stretching of the rock at very high strains. This process is inevitably associated with a grain boundary sliding mechanism and diffusion dominated creep. The growth of albite and quartz rims around the K-feldspar grains and the overall grain size increase of both feldspars can result from the above mentioned mass transfer mechanisms.

[47] The intensity of quartz CPO in Type III microstructures decreases compared to Type II microstructures. This is due to a switch of the active slip system from prism < a > toward basal < a > and rhomb < a + c > slip systems in Type III microstructure (Figure 15c). These slip systems are not common in partially molten high-grade mylonites where the activity of prism < c > glide is reported [e.g., *Gapais and Barbarin*, 1986; *Martelat et al.*, 1999]. Our observations do not indicate a late reworking during a low-temperature event and we therefore suggest that the activity of the "low-temperature" slip systems in high-grade mylonites results from strain rate or stress conditions which are currently unconstrained [*Závada et al.*, 2007; *Hasalová et al.*, 2008]. Consequently, the deformation mechanism in quartz is the dislocation creep and the evolution of slip systems suggest a decrease of the flow stress or strain rate compared to previous stages [*Handy*, 1990; *Herwegh et al.*, 1997; *Schmid and Casey*, 1986]. However, the diffusional creep in the feldspar matrix supported by grain shapes and crystallographic preferred orientations (Figure 13) shows that the Type III microstructures represent a deformation stage marked by the overall flow stress drop associated with the increase of homogeneity of the strain distribution. This overall weakening is consistent with interstitial phases forming a substantial proportion of the rock volume and shapes of pools or thick films of Pl2 and quartz grains that are similar to the melt topology described by *Sawyer* [2001] or *Marchildon and Brown* [2003].

8.6. Quantitative Microstructural and Petrological Arguments for Syn-deformational Melting

[48] The CSD curves (Figure 9b) show decreasing N_0 and increasing G_t values in relict plagioclase aggregates toward Type III rocks. The trend from Type II to Type III rocks (Figure 9b) consistent with the rapid nucleation of interstitial Pl2 is marked by the presence of thin isolated films in SEM images of Type II microstructures (Figure 6, samples T1 and M2, and Figure 8). The decrease of N_0 and increase of G_t values in Type III microstructures correspond to a growth of Pl2 pools and large new Pl2 rims in a K-feldspar dominated matrix (Figure 7, samples V1 and D1). This evolution corrobarates the weakening of the aggregate distribution in Type II microstructures toward an almost random distribution in Type III microstructures and an associated development of important proportion of the interstitial phases (Figure 11).

[49] The pseudosection modeling indicates that the only fluid that could be present during the deformation of the orthogneiss at the estimated temperatures of 650–680°C is a silicate melt (Figure 14). Either the temperature increase or the pressure drop along the path estimated by *Pitra and Guiraud* [1996] or *Tajcmanová et al.* [2006] for associated metapelites can be responsible for the dehydration melting of the muscovite-biotite bearing orthogneiss assemblage. The amount of melting may even be increased by external fluids introduced from the surrounding metapelites [*Thompson and Connolly*, 1995].

[50] The nucleation dominated part of the deformation-melting history in Type II microstructures is probably associated with the onset of the melting reaction and heterogeneous nucleation of the melt droplets at high-energy triple points or noncoherent grain boundaries. The growth dominated process associated with the Type III microstructures reflects a more advanced melting leading to the development of large pools and the coalescence of small nuclei along all boundaries in deformed aggregates. This process is best exemplified by the sample B2 which resembles a migmatitic structure at the macroscopic scale.

8.7. Grain Boundary Sliding Diffusional Creep and Variations in Melt Topology With Increasing Melt Fraction

[51] The studied microstructural sequence is characterized by the increasing deformation intensity (Figure 3), the increasing melt fraction (Figures 4, 6, and 7), grain size (Figure 9) and random grain contact distribution as well as the low aspect ratio of grains (Figures 10 and 11). This evolutionary trend is accompanied by a change in orientation of the melt seams (Figures 8 and 16) from an orientation subparallel to the foliation to seams oriented at high angle to the foliation.

[52] Melt seams preferentially located along grain boundaries parallel to the foliation in Type II microstructures are commonly reported in natural samples [*Sawyer*, 2001; *Rosenberg and Berger*, 2001] and in some experimental or analog studies [*Daines and Kohlstedt*, 1997; *Groebner and Kohlstedt*, 2006; *Walte et al.*, 2005]. This geometry can be observed in microstructures of the T1 and T2 samples and is compatible with the combined activity of grain boundary sliding and crystal-plastic deformation mechanisms at very low melt fractions (<2%). Therefore, the

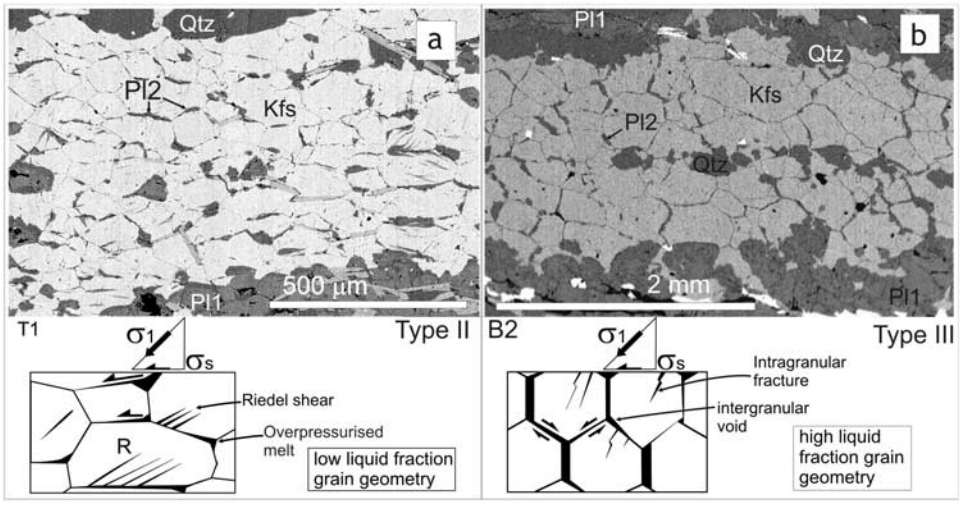

Figure 16. The evolution of (a) shear plane-parallel melt preferred orientation at low melt fractions and (b) shear plane-perpendicular melt preferred orientation at high melt fractions. At low melt fractions, shear is accommodated by the grain boundary sliding parallel to the shear direction. Since grain boundary sliding means a loss of the cohesion along these boundaries, they represent an easy path for melt which accumulates at these boundaries (bottom left, Figure 16a). At higher melt fractions, a switch from shear plane parallel to shear plane-perpendicular melt preferred orientation can be observed. This is probably because of stress concentrations at grain boundaries oriented perpendicular to simple shear and accompanying dilation/cavitation of these boundaries (bottom right, Figure 16b). See text for further explanations.

orientation of melt seams can be explained by a loss of cohesion at boundaries oriented parallel to the foliation. Because of shearing, the melt concentrated at triple points suffers an increasing overpressure. We suggest that the combination of loss of cohesion and build up of melt overpressure leads to the injection of melt between actively moving grain boundaries oriented at a high angle to the principal compressive stress, i.e., parallel to the macroscopic foliation (Figure 16a). Oblique intragranular fractures can be interpreted as Riedel shears channeling melt from overpressured, dilatant grain boundaries accompanying movements along foliation-parallel grain boundaries [*Rosenberg and Handy*, 2000]. The M1 and M2 samples are characterized by a general constrictional deformation, lower aspect ratio of grains and low melt fraction (<2%). Similarly to the T1 and T2 samples these grain aggregates exhibit microscopic features compatible with grain boundary sliding and plastic deformation. The preferred orientation of melt is weaker compared to the T1 and T2 samples, which can be explained by a smaller dimension of active grain boundaries and also by a prolate shape of the strain ellipsoid.

[53] The overpressured melt is therefore injected in between grain boundaries of variable orientation with a mean direction parallel to the foliation. This orientation is therefore a function of (1) melt fraction, where little melt behaves as isolated weak pockets localizing strain (Figure 16a); and (2) deformation mechanisms probably corresponding to the grain boundary sliding–grain boundary locking transitional regime defined by *Walte et al.* [2005]. This regime is marked by the transition from grain boundary sliding to crystal-plastic framework deformation promoting foliation parallel to the elongation associated with the development of a strong melt preferred orientation parallel to the principal stretching direction [*Groebner and Kohlstedt*, 2006].

[54] In Type III microstructures (samples R3, V1, B2) the melt pools and intragranular melt filled fractures are oriented at a high angle to the stretching direction but show rather weak preferred orientations (Figure 16b). Experimental studies by *Dell'Angelo et al.* [1987] and *Dell'Angelo and Tullis* [1988] show that melt pockets are perpendicular to the maximum stress direction for high differential stress and relatively low melt fractions of 3–5%. Analogue studies of *Walte et al.* [2005] and *Park and Means* [1996] show comparable development of melt pockets oriented parallel to the principal stress at melt fractions ranging from 4 to 10%. Consequently, we suggest that the Type III microstructures result from the distributed granular flow, which operated at higher melt fractions between 5–10%, and where the higher melt fraction and connectivity promote grain boundary sliding and dynamic dilation (Figure 16b).

[55] *Závada et al.* [2007] explain the development of melt films perpendicular to the stretching direction by the mechanisms of intergranular and/or intragranular fracturing during grain boundary sliding at melt fractions between 2–5%. They propose that the dilation represents a final creep failure state which resulted from a cavitation process accompanying the grain boundary sliding controlled diffusion creep. They also suggested that, in analogy to the experimental works of *Sklenička et al.* [1977] and *Kassner and Hayes* [2003]; the distributed intergranular cavitation in K-feldspar is consistent with relatively slow strain rates typical for diffusion type creep. Another possible model proposes that the melt is overpressured and therefore can overcome the least principal stress as well as the cohesion of

suitably oriented planes in the aggregate [*Hubbert and Rubey*, 1959]. As a result of melt overpressure, the feldspar aggregate dilates and the melt is accumulated in intergranular and intragranular pockets and fractures.

[56] It is likely that the evolution in the orientation of melt pockets is caused by the increasing melt fraction and/or by the change in differential stress magnitude and orientation [*Cosgrove*, 1997]. The implication of the increasing melt fraction and connectivity certainly influences the distribution of local compressive and shear stress magnitudes and orientations and the active deformation mechanism (Figure 16). In this context, it is not likely that the melt preferred orientation is controlled by the variations in differential stress [*Gleason et al.*, 1999], hydrostatic annealing [*Daines and Kohlstedt*, 1997] or variations in the wetting angle [*Walte et al.*, 2005]. In order to further explain this relationship between melt seam orientations and melt fractions more analogs and possibly numerical modeling is needed.

[57] In Type II microstructures the diffusion creep rates of both feldspars were effectively enhanced by the interstitial melt phase wetting their boundaries and leading to a rapid strength drop within the MCT field as proposed by [*Rosenberg and Handy*, 2005]. This is consistent with a low amount of melt <2% produced by the continuous metamorphic reaction in the absence of externally introduced fluid as inferred from petrological modeling. However, Type III microstructures are characterized by higher proportions of melt which can be produced by the introduction of external fluids into the system. The increase of the melt fraction is responsible for a substantial modification of the bulk deformation mechanism from crystalline plasticity assisted grain boundary sliding to granular flow.

9. Conclusions

[58] 1. Extreme weakness of feldspars is reported in midcrustal granite mylonite which is marked by disproportionately higher strain intensities of the feldspar polycrystalline aggregates compared to quartz.

[59] 2. Three types of microstructures corresponding to the evolutionary stages of deformed granite were recognized: Type I (metagranite marked by a viscous flow of plagioclase around the strong alkali feldspar and quartz), Type II (quartz augen orthogneiss characterized by the development of a banded mylonitic structure of recrystallized plagioclase and K-feldspar surrounding augens of quartz), and Type III (banded orthogneiss characterized by the alternation of quartz ribbons and mixed aggregates of feldspars and quartz).

[60] 3. The weakening of the alkali feldspar is achieved by the decomposition into albite chains and K-feldspar resulting from a heterogeneous nucleation process.

[61] 4. The extreme deformation of feldspars and their progressive mixing are attributed to syn-deformational melting of muscovite-biotite rich layers associated with the grain boundary sliding controlled diffusion creep of feldspars.

[62] 5. The strong quartz shows a dislocation creep deformation mechanism throughout the deformation history marked by the variations in activity of the slip systems, which are attributed to variations in the stress and strain rate partitioning with regard to changing rheological properties of the deforming feldspars.

[63] 6. The orientation of melt seams varies with increasing strain; this can be explained as a consequence of a concomitant increase in the melt fraction associated with a change in the far field and local stress field conditions.

[64] **Acknowledgments.** The grant to Stanislav Ulrich of the Research Council of the Czech Academy of Science is gratefully acknowledged. This study was made possible thanks to the ANR project "LFO in Orogens" funding as well as to financial support of CNRS (UMRs 7516 and 7517). We are grateful to Ed Sawyer and Denis Gapais for fruitful and constructive reviews.

References

Baratoux, L., K. Schulmann, S. Ulrich, and O. Lexa (2005), Contrasting microstructures and deformation mechanisms in metagabbro mylonites contemporaneously deformed under different temperatures (c. 650°C and c. 750°C), in *Deformation Mechanisms, Rheology and Tectonics: From the Minerals to the Lithosphere*, edited by D. Gapais, J. P. Brun, and P. R. Cobbold, *Geol. Soc. Spec. Publ.*, *243*, 97–125.

Bascou, J., G. Barruol, A. Vauchez, D. Mainprice, and M. Egydio-Silva (2001), EBSD-measured lattice-preferred orientations and seismic properties of eclogites, *Tectonophysics*, *342*, 61–80, doi:10.1016/S0040-1951(01)00156-1.

Beneš, K. (1964), Geologická mappá ČSSR, map, scale 1:200,000, Ústřední Ústav Geol., Prague.

Boullier, A. M., and Y. Guéguen (1975), SP-Mylonites: Origin of some mylonites by superplastic flow, *Contrib. Mineral. Petrol.*, *50*, 93–104, doi:10.1007/BF00373329.

Carter, N. L., and M. Tsenn (1987), Flow properties of continental lithosphere, *Tectonophysics*, *136*, 27–63, doi:10.1016/0040-1951(87)90333-7.

Cashman, K. V., and J. M. Ferry (1988), Crystal size distribution (CSD) in rocks and the kinetics and dynamics of crystallization III. Metamorphic crystallization, *Contrib. Mineral. Petrol.*, *99*, 401–415, doi:10.1007/BF00371933.

Coggon, R., and T. J. B. Holland (2002), Mixing properties of phengitic micas and revised garnet-phengite thermobarometers, *J. Metamorph. Geol.*, *20*, 683–696, doi:10.1046/j.1525-1314.2002.00395.x.

Cosgrove, J. W. (1997), The influence of mechanical anisotropy on the behaviour of the lower crust, *Tectonophysics*, *280*, 1–14.

Daines, M. J., and D. L. Kohlstedt (1997), Influence of deformation on melt topology in peridotites, *J. Geophys. Res.*, *102*, 10,257–10,272, doi:10.1029/97JB00393.

Dallain, C., K. Schulmann, and P. Ledru (1999), Textural evolution in the transition from subsolidus annealing to melting process, Velay Dome, French Massif Central, *J. Metamorph. Geol.*, *17*, 61–74, doi:10.1046/j.1525-1314.1999.00176.x.

Dell'Angelo, L. N., and J. Tullis (1988), Experimental deformation of partially melted granitic aggregates, *J. Metamorph. Geol.*, *6*, 495–515, doi:10.1111/j.1525-1314.1988.tb00436.x.

Dell'Angelo, L. N., and J. Tullis (1996), Textural and mechanical evolution with progressive strain in experimentally deformed aplite, *Tectonophysics*, *256*, 57–82, doi:10.1016/0040-1951(95)00166-2.

Dell'Angelo, L. N., J. Tullis, and R. A. Yund (1987), Transition from dislocation creep to melt-enhanced diffusion creep in fine-grained granitic aggregates, *Tectonophysics*, *139*, 325–332, doi:10.1016/0040-1951(87)90107-7.

Eudier, M. (1962), Mechanical properties of sintered low-alloy steels, *Powder Metall.*, *9*, 278–290.

Fitz Gerald, J. D., and H. Stünitz (1993), Deformation of granitoids at low metamorphic grades. I. Reactions and grainsize reduction, *Tectonophysics*, *221*, 269–297, doi:10.1016/0040-1951(93)90163-E.

Flinn, D. (1965), On the symmetry principle and the deformation ellipsoid, *Geol. Mag.*, *102*, 36–45.

Flinn, D. (1969), Grain contacts in crystalline rocks, *Lithos*, *3*, 361–370.

Franěk, J., K. Schulmann, and O. Lexa (2006), Kinematic and rheological model of exhumation of high pressure granulites in the Variscan orogenic root: Example of the Blanský les granulite, Bohemian Massif, Czech Republic, *Mineral. Petrol.*, *86*, 253–276, doi:10.1007/s00710-005-0114-4.

Gapais, D. (1989), Shear structures within deformed granites; mechanical and thermal indicators, *Geology*, *17*, 1144–1147, doi:10.1130/0091-7613(1989)017<1144:SSWDGM>2.3.CO;2.

Gapais, D., and B. Barbarin (1986), Quartz fabric transition in a cooling syntectonic granite (Hermitage massif, France), *Tectonophysics*, *125*, 357–370, doi:10.1016/0040-1951(86)90171-X.

Gay, N. C. (1968a), Pure shear and simple shear deformation of inhomogeneous viscous fluids. 1. Theory, *Tectonophysics*, *5*, 211–234, doi:10.1016/0040-1951(68)90065-6.

Gay, N. C. (1968b), Pure shear and simple shear deformation of inhomogeneous viscous fluids. 2. The deformation of the total finite strain in a rock from objects such as deformed pebbles, *Tectonophysics*, *5*, 295–302, doi:10.1016/0040-1951(68)90033-4.

Gleason, G. C., V. Bruce, and H. W. Green (1999), Experimental investigation of melt topology in partially molten quartzo-feldspathic aggregates under hydrostatic and non-hydrostatic stress, *J. Metamorph. Geol.*, *17*, 705–722, doi:10.1046/j.1525-1314.1999.00228.x.

Groebner, N., and D. L. Kohlstedt (2006), Deformation induced metal melt networks in silicates: Implications for core-mantle interactions in planetary bodies, *Earth Planet. Sci. Lett.*, *245*, 571–580, doi:10.1016/j.epsl.2006.03.029.

Handy, M. R. (1990), The solid-state flow of polymineralic rocks, *J. Geophys. Res.*, *95*, 8647–8661, doi:10.1029/JB095iB06p08647.

Handy, M. R. (1994a), The energetics of steady-state heterogeneous shear in mylonitic rock, *Mater. Sci. Eng. A*, *175*, 261–272, doi:10.1016/0921-5093(94)91065-0.

Handy, M. R. (1994b), Flow laws for rocks containing two non-linear viscous phases: A phenomenological approach, *J. Struct. Geol.*, *16*, 287–301, doi:10.1016/0191-8141(94)90035-3.

Handy, M. R., S. Wissing, and J. E. Streit (1999), Strength and structure of mylonite with combined frictional-viscous rheology and varied bimineralic composition, *Tectonophysics*, *303*, 175–191, doi:10.1016/S0040-1951(98)00251-0.

Hasalová, P., K. Schulmann, O. Lexa, P. Štípská, and F. Hrouda (2008), Origin of felsic migmatites by progressive destruction of metamorphic layering during ductile shearing and melt infiltration, *J. Metamorph. Geol.*, *26*, 29–53.

Heilbronner, R., and J. Tullis (2006), Evolution of c axis pole figures and grain size during dynamic recrystallization: Results from experimentally sheared quartzite, *J. Geophys. Res.*, *111*, B10202, doi:10.1029/2005JB004194.

Herwegh, M., M. R. Handy, and R. Heilbronner (1997), Temperature- and strain-rate-dependent microfabric evolution in monomineralic mylonite: Evidence from in situ deformation of norcamphor, *Tectonophysics*, *280*, 83–106, doi:10.1016/S0040-1951(97)00139-X.

Higgins, M. D. (1998), Origin of anorthosite by textural coarsening: Quantitative measurements of a natural sequence of textural development, *J. Petrol.*, *39*, 1307–1325, doi:10.1093/petrology/39.7.1307.

Hobbs, B. E. (1981), The influence of metamorphic environment upon the deformation of minerals, *Tectonophysics*, *78*, 335–383, doi:10.1016/0040-1951(81)90020-2.

Holland, T. J. B., and R. Powell (1998), An internally consistent thermodynamic data set for phases of petrological interest, *J. Metamorph. Geol.*, *16*, 309–343, doi:10.1111/j.1525-1314.1998.00140.x.

Holland, T. J. B., and R. Powell (2003), Activity-composition relations for phases in petrological calculations: An asymmetric multicomponent formulation, *Contrib. Mineral. Petrol.*, *145*, 492–501, doi:10.1007/s00410-003-0464-z.

Hubbert, M. K., and W. W. Rubey (1959), Role of fluid pressure in mechanics of overthrust faulting, *Geol. Soc. Am. Bull.*, *70*, 116–166.

Jaoul, O., J. Tullis, and A. Kronenberg (1984), The effect of varying water contents on the creep behavior of Heavitree Quartzite, *J. Geophys. Res.*, *89*, 4298–4312, doi:10.1029/JB089iB06p04298.

Ji, S., and P. Zhao (1994), Strength of two-phase rocks: A model based on fiber-loading theory, *J. Struct. Geol.*, *16*, 253–262, doi:10.1016/0191-8141(94)90108-2.

Ji, S., R. Wirth, E. Rybacki, and J. Zhenting (2000), High-temperature plastic deformation of quartz-plagioclase multilayers by layer-normal compression, *J. Geophys. Res.*, *105*, 16,651–16,664, doi:10.1029/2000JB900130.

Jordan, P. G. (1987), The deformational behaviour of bimineralic limestone-halite aggregates, *Tectonophysics*, *135*, 185–197, doi:10.1016/0040-1951(87)90160-0.

Jordan, P. G. (1988), The rheology of polymineralic rocks — An approach, *Geol. Rundsch.*, *77*, 285–294, doi:10.1007/BF01848690.

Kachlík, V. (1999), Relationship between Maldanubicum (Central Bohemia, Czech Republic): A result of the polyphase Variscan nappe tectonics, *J. Czech Geol. Soc.*, *44*, 201–291.

Kassner, M. E., and T. A. Hayes (2003), Creep cavitation in metals, *Int. J. Plast.*, *19*, 1715–1748, doi:10.1016/S0749-6419(02)00111-0.

Kretz, R. (1969), On the spatial distribution of crystals in rocks, *Lithos*, *2*, 39–66, doi:10.1016/S0024-4937(69)80005-8.

Kretz, R. (1983), Symbols for rock-forming minerals, *Am. Mineral.*, *68*, 277–279.

Kronenberg, A., and J. Tullis (1984), Flow strengths of quartz aggregates; grain size and pressure effects due to hydrolytic weakening, *J. Geophys. Res.*, *89*, 4281–4297, doi:10.1029/JB089iB06p04281.

Kruhl, J. H. (1996), Prism- and basal-plane parallel subgrain boundaries in quartz: A microstructural geothermobarometer, *J. Metamorph. Geol.*, *14*, 581–589, doi:10.1046/j.1525-1314.1996.00413.x.

Kruse, R., and H. Stünitz (1999), Deformation mechanisms and phase distribution in mafic high-temperature mylonites from the Jotun Nappe, southern Norway, *Tectonophysics*, *303*, 223–249, doi:10.1016/S0040-1951(98)00255-8.

Kruse, R., H. Stünitz, and K. Kunze (2001), Dynamic recrystallization processes in plagioclase porphyroclast, *J. Struct. Geol.*, *23*, 1781–1802, doi:10.1016/S0191-8141(01)00030-X.

Lexa, O., P. Štípská, K. Schulmann, L. Baratoux, and A. Kröner (2005), Contrasting textural record of two distinct metamorphic events of similar P-T conditions and different durations, *J. Metamorph. Geol.*, *23*, 649–666, doi:10.1111/j.1525-1314.2005.00601.x.

Marchildon, N., and M. Brown (2003), Spatial distribution of melt-bearing structures in anatectic rocks from Southern Brittany: Implications for melt-transfer at grain- to orogen-scale, *Tectonophysics*, *364*, 215–235, doi:10.1016/S0040-1951(03)00061-1.

Martelat, J.-E., K. Schulmann, J.-M. Lardeaux, and C. Nicollet (1999), Granulite microfabric and deformation mechanisms in southern Madagascar, *J. Struct. Geol.*, *21*, 671–687, doi:10.1016/S0191-8141(99)00052-8.

McLellan, E. L. (1983), Contrasting textures in metamorphic and anatectic migmatites: An example from the Scottish Caledonides, *J. Metamorph. Geol.*, *1*, 241–262, doi:10.1111/j.1525-1314.1983.tb00274.x.

Medaris, L. G., J. H. Fournelle, E. D. Ghent, E. Jelínek, and Z. Mísař (1998), Prograde eclogite in the Gföhl Nappe, Czech Republic: New evidence on Variscan high-pressure metamorphism, *J. Metamorph. Geol.*, *16*, 563–576, doi:10.1111/j.1525-1314.1998.00158.x.

Montardi, Y., and D. Mainprice (1987), A transmission electron microscopic study of the plastic deformation of calcic plagioclase (An 68–70), *Bull. Mineral.*, *110*, 1–14.

Olsen, T. S., and D. L. Kohlstedt (1985), Natural deformation and recrystalization of some intermediate plagioclase feldspars, *Tectonophysics*, *111*, 107–131, doi:10.1016/0040-1951(85)90067-8.

Park, Y., and W. D. Means (1996), Direct observation of deformation processes in crystal mushes, *J. Struct. Geol.*, *18*, 847–858, doi:10.1016/S0191-8141(96)80017-4.

Peterson, T. D. (1996), A refined technique for measuring crystal size distributions in thin section, *Contrib. Mineral. Petrol.*, *124*, 395–405, doi:10.1007/s004100050199.

Pitra, P., and M. Guiraud (1996), Probable anticlockwise P-T evolution in extending crust: Hlinsko region, Bohemian Massif, *J. Metamorph. Geol.*, *14*, 49–60, doi:10.1111/j.1525-1314.1996.t01-1-00049.x.

Powell, R., and T. J. B. Holland (2004), Course notes for "THERMOCALC Workshop 2004: Calculating metamorphic phase equilibria [CD-ROM], report, Eidg. Tech. Hochsch., Zurich, Zurich, Switz.

Powell, R., T. Holland, and B. Worley (1998), Calculating phase diagrams involving solid solutions via non-linear equations, with examples using THERMOCALC, *J. Metamorph. Geol.*, *16*, 577–588, doi:10.1111/j.1525-1314.1998.00157.x.

Putnis, A., C. M. Pina, J. M. Astilleros, L. Fernández-Díaz, and M. Prieto (2003), Nucleation of solid solutions crystallizing from aqueous solutions, *Philos. Trans. R. Soc. London, Ser. A*, *361*, 615–632, doi:10.1098/rsta.2002.1142.

Ramsay, J. G., and M. I. Huber (1983), *The Techniques of Modern Structural Geology*, vol. 1, *Strain Analysis*, 307 pp., Elsevier, London.

Ranalli, G. (1995), *Rheology of the Earth*, 2nd ed., 366 pp., CRC Press, London.

Ranalli, G., and D. C. Murphy (1987), Rheological stratification of the lithosphere, *Tectonophysics*, *132*, 281–295, doi:10.1016/0040-1951(87)90348-9.

Randolph, A. D., and M. A. Larson (1971), *Theory of Particle Processes*, 251 pp., Elsevier, San Diego, Calif.

Ribbe, P. H. (1983), Chemistry structure and nomenclature of feldspars, in *Feldspar Mineralogy*, *Rev. Mineral.*, vol. 2, 2nd ed., edited by P. H. Ribbe, pp. 21–55, Mineral. Soc. of Am., Washington, D. C.

Rosenberg, C. L., and A. Berger (2001), Syntectonic melt pathways in granite, and melt-induced transition in deformation mechanisms, *Phys. Chem. Earth, Part A*, *26*, 287–293.

Rosenberg, C. L., and M. R. Handy (2000), Syntectonic melt pathways during simple shearing of a partially molten rock analogue (Norcamphor-Benzamide), *J. Geophys. Res.*, *105*, 3135–3149, doi:10.1029/1999JB900371.

Rosenberg, C. L., and M. R. Handy (2005), Experimental deformation of partially melted granite revisited: Implications for the continental crust,

J. Metamorph. Geol., *23*, 19–28, doi:10.1111/j.1525-1314.2005.00555.x.

Rybacki, E., and G. Dresen (2004), Deformation mechanism maps for feldspar rocks, *Tectonophysics*, *382*, 173–187, doi:10.1016/j.tecto.2004.01.006.

Sawyer, E. W. (2001), Melt segregation in the continental crust: Distribution and movement of melt in anatectic rocks, *J. Metamorph. Geol.*, *19*, 291–309, doi:10.1046/j.0263-4929.2000.00312.x.

Scaillet, B., C. France-Lanord, and P. Le Fort (1990), Badrinath-Gangotri plutons (Garhwal, India): Petrological and geochemical evidence for fractionation processes in a high Himalayan leucogranite, *J. Volcanol. Geotherm. Res.*, *44*, 163–188, doi:10.1016/0377-0273(90)90017-A.

Schmid, S. M. (1982), Microfabric studies as indicators of deformation mechanisms and flow laws operative in mountain building, in *Mountain Building Processes*, edited by K. J. Hsü, pp. 95–110, Elsevier, London.

Schmid, S. M., and M. Casey (1986), Complete fabric analysis of some commonly observed quartz c-axis patterns, in *Mineral and Rock Deformation: Laboratory Studies*, *Geophys. Monogr. Ser.*, vol. 36, edited by B. E. Hobbs and H. C. Heard, pp. 263–286, AGU, Washington, D. C.

Schmid, S. M., R. Panozzo, and S. Bauer (1987), Simple shear experiments on calcite rocks: Rheology and microfabric, *J. Struct. Geol.*, *9*, 747–778, doi:10.1016/0191-8141(87)90157-X.

Schmid, S. M., R. Heilbronner, and H. Stünitz (1999), Deformation mechanisms in nature and experiment (editorial remarks), *Tectonophysics*, *303*, vii–ix, doi:10.1016/S0040-1951(98)00302-3.

Schulmann, K., B. Mlcoch, and R. Melka (1996), High-temperature microstructures and rheology of deformed granite, Erzgebirge, Bohemian Massif, *J. Struct. Geol.*, *18*, 719–733, doi:10.1016/S0191-8141(96)80007-1.

Schulmann, K., A. Kröner, E. Hegner, I. Wendt, J. Konopásek, O. Lexa, and P. Štípská (2005), Chronological constraints on the pre-orogenic history, burial and exhumation of deep-seated rocks along the eastern margin of the Variscan Orogen, Bohemian Massif, Czech Republic, *Am. J. Sci.*, *305*, 407–448, doi:10.2475/ajs.305.5.407.

Simpson, C. (1985), Deformation of granitic rocks across the brittle-ductile transition, *J. Struct. Geol.*, *7*, 503–511, doi:10.1016/0191-8141(85)90023-9.

Sklenička, V., J. Saxl, and J. Čadek (1977), Intercrystalline fracturing at high temperature creep of metals and alloys (in Czech), report, 108 pp., Czech. Acad. of Sci., Prague.

Stünitz, H., and J. D. Fitz Gerald (1993), Deformation of granitoids at low metamorphic grades. II. Granular flow in albite-rich mylonites, *Tectonophysics*, *221*, 299–324, doi:10.1016/0040-1951(93)90164-F.

Synek, J., and D. Oliverová (1993), Terrane character of the north-east margin of the Moldanubian Zone: The Kutná Hora Crystalline Complex, Bohemian Massif, *Geol. Rundsch.*, *82*, 566–582, doi:10.1007/BF00212417.

Tajcmanová, L., J. Konopásek, and K. Schulmann (2006), Thermal evolution of the orogenic lower crust during exhumation within a thickened Moldanubian root of the Variscan belt of Central Europe, *J. Metamorph. Geol.*, *24*, 119–134, doi:10.1111/j.1525-1314.2006.00629.x.

Tharp, T. M. (1983), Analogies between the high-temperature deformation of polyphase rocks and the mechanical behavior of porous powder metal, *Tectonophysics*, *96*, 1–11, doi:10.1016/0040-1951(83)90216-0.

Thompson, A. B., and J. A. D. Connolly (1995), Melting of the continental crust: Some thermal and petrological constraints on anatexis in continental collision zones and other tectonic settings, *J. Geophys. Res.*, *100*, 15,565–15,580, doi:10.1029/95JB00191.

Treagus, S. H. (2002), Modelling the bulk vicosity of two-phase mixtures in term of clast shape, *J. Struct. Geol.*, *24*, 57–76, doi:10.1016/S0191-8141(01)00049-9.

Tullis, J. (1983), Deformation of feldspars, in *Feldspar Mineralogy*, *Rev. Mineral.*, vol. 2, 2nd ed., edited by P. H. Ribbe, pp. 297–323, Mineral. Soc. of Am., Washington, D. C..

Tullis, J. (1990), Experimental studies of deformation mechanisms and microstructures in quartzo-feldspathic rocks, in *Deformation Processes in Minerals, Ceramics and Rocks*, edited by D. Barbour and P. Meredith, pp.190–227, CRC Press, Cambridge, U. K.

Walte, N. P., P. D. Bons, and C. W. Passchier (2005), Deformation of melt-bearing systems — Insight from in situ grain-scale analogue experiments, *J. Struct. Geol.*, *27*, 1666–1679, doi:10.1016/j.jsg.2005.05.006.

White, J. C., and C. K. Mawer (1986), Extreme ductility of feldspars from a mylonite, Parry Sound, Canada, *J. Struct. Geol.*, *8*, 133–143, doi:10.1016/0191-8141(86)90104-5.

White, J. C., and C. K. Mawer (1988), Dynamic recrystallization and associated in perthites: Evidence of deep crustal thrusting, *J. Geophys. Res.*, *93*, 325–337, doi:10.1029/JB093iB01p00325.

White, R. W., R. Powell, and T. J. B. Holland (2001), Calculation of partial melting equilibria in the system $Na_2O-CaO-K_2O-FeO-MgO-Al_2O_3-SiO_2-H_2O$ (NCKFMASH), *J. Metamorph. Geol.*, *19*, 139–153, doi:10.1046/j.0263-4929.2000.00303.x.

Závada, P., K. Schulmann, J. Konopásek, O. Lexa, and S. Ulrich (2007), Melt topology in deformed quartzo-feldspathic rocks: Implication for rheology and grain-scale migration of melt in partially molten crust, *J. Geophys. Res.*, *112*, B10210, doi:10.1029/2006JB004820.

J. K. Becker, Institut für Geowissenschaften, Universität Tübingen, Sigwartstrasse 10, D-72076 Tübingen, Germany.

O. Lexa, Institute of Petrology and Structural Geology, Charles University, Albertov 6, 12843 Praha 2, Czech Republic.

J.-E. Martelat, Laboratoire de Géodynamique des Chaînes Alpines, UMR5025, Université Joseph Fourier, Observatoire des Sciences de l'Univers de Grenoble, CNRS, F-38041 Grenoble Cedex 9, France.

K. Schulmann and P. Štípská, Centre de Géochimie de la Surface, UMR7516, Université Louis Pasteur, CNRS, F-67084 Strasbourg Cedex, France.

S. Ulrich, Geophysical Institute, Czech Academy of Sciences, Bočni II/1401, 14131 Praha 4, Czech Republic.